Journal of Geophysical Research: Planets

RESEARCH ARTICLE
10.1002/2014JE004661

# Geophysical evidence for melt in the deep lunar interior and implications for lunar evolution

**A. Khan**[1], **J. A. D. Connolly**[2], **A. Pommier**[3], **and J. Noir**[1]

[1]Institute of Geophysics, ETH Zürich, Zurich, Switzerland, [2]Institute of Geochemistry and Petrology, ETH Zürich, Zurich, Switzerland, [3]Institute of Geophysics and Planetary Physics, Scripps Institution of Oceanography, University of California, San Diego, La Jolla, California, USA

**Key Points:**
- We investigate deep lunar thermochemical structure using geophysical data
- An FeO- and $TiO_2$-enriched melt layer is required by data at depths >1200 km
- Results strongly constrain models of lunar thermal evolution

**Correspondence to:**
A. Khan,
amir.khan@erdw.ethz.ch

**Citation:**
Khan, A., J. A. D. Connolly, A. Pommier, and J. Noir (2014), Geophysical evidence for melt in the deep lunar interior and implications for lunar evolution, *J. Geophys. Res. Planets*, *119*, doi:10.1002/2014JE004661.

Received 4 MAY 2014
Accepted 11 SEP 2014
Accepted article online 18 SEP 2014

**Abstract** Analysis of lunar laser ranging and seismic data has yielded evidence that has been interpreted to indicate a molten zone in the lowermost mantle overlying a fluid core. Such a zone provides strong constraints on models of lunar thermal evolution. Here we determine thermochemical and physical structure of the deep Moon by inverting lunar geophysical data (mean mass and moment of inertia, tidal Love number, and electromagnetic sounding data) in combination with phase-equilibrium computations. Specifically, we assess whether a molten layer is required by the geophysical data. The main conclusion drawn from this study is that a region with high dissipation located deep within the Moon is required to explain the geophysical data. This region is located within the mantle where the solidus is crossed at a depth of ∼1200 km (≥1600°C). Inverted compositions for the partially molten layer (150–200 km thick) are enriched in FeO and $TiO_2$ relative to the surrounding mantle. The melt phase is neutrally buoyant at pressures of ∼4.5–4.6 GPa but contains less $TiO_2$ (<15 wt %) than the Ti-rich (∼16 wt %) melts that produced a set of high-density primitive lunar magmas (density of 3.4 g/cm$^3$). Melt densities computed here range from 3.25 to 3.45 g/cm$^3$ bracketing the density of lunar magmas with moderate-to-high $TiO_2$ contents. Our results are consistent with a model of lunar evolution in which the cumulate pile formed from crystallization of the magma ocean as it overturned, trapping heat-producing elements in the lower mantle.

## 1. Introduction

The structure of the deep lunar interior is intimately linked to the large-scale evolution of the Moon and therefore holds the potential of constraining its compositional and thermal evolution. An illustration of this linkage is the idea that toward the end of lunar magma ocean crystallization dense titanium-rich cumulates formed near the base of the crust [*Kesson and Ringwood*, 1976]. This dense cumulate pile is eventually supposed to have become gravitationally unstable whereupon the $TiO_2$-rich phases settled toward the bottom of the mantle as a result of convective overturn [e.g., *Taylor and Jakes*, 1974; *Snyder et al.*, 1992; *Hess and Parmentier*, 1995; *Wagner and Grove*, 1997; *Elkins-Tanton et al.*, 2002] where they remain partially molten due to a high complement of trapped heat-producing elements [*de Vries et al.*, 2010]. Thus, evidence for a deep lunar melt layer would support this evolutionary model.

The absence of recent volcanic activity suggests that if partial melt is present deep within the Moon, it must be at least as dense as the surrounding mantle [e.g., *Delano*, 1990]. This has led several workers to experimentally investigate samples collected during the Apollo missions that are thought to have formed in volcanic eruptions on the lunar surface [*Elkins-Tanton et al.*, 2003]. These samples represent the most primitive lunar magmas to have been collected to date [e.g., *Delano*, 1986]. Analyses showed that only the most $TiO_2$-rich primitive lunar melts, corresponding to Apollo 14 black glass (∼16 wt % $TiO_2$), would be neutrally buoyant with respect to the lunar mantle [e.g., *Delano*, 1990; *Circone and Agee*, 1996; *Smith and Agee*, 1997; *Sakamaki et al.*, 2010; *van Kan Parker et al.*, 2011, 2012]. This observation has fueled speculation that the source of pristine mare glasses, considered to be the best candidates for lunar primary magmas [*Delano*, 1986], could be related to the melt-bearing layer. However, given the unknown chemical composition and density of the deep melt, the generic link to the source of primary magmas is hypothetical.

In spite of geophysical evidence bearing on the deep lunar interior, details remain perfunctory largely as a result of the indirect nature of the data available. Lunar laser ranging (LLR) [e.g., *Williams et al.*, 2001, 2012, 2014] and gravity data from orbiting spacecraft [e.g., *Yan et al.*, 2011; *Goossens et al.*, 2011; *Konopliv et al.*, 2013; *Lemoine et al.*, 2013] suggest the presence of an attenuating region deep within the Moon in line with conclusions drawn from analysis of dissipation-related data [e.g., *Williams et al.*, 2001, 2014; *Khan and Mosegaard*, 2005; *Efroimsky*, 2012; *Harada et al.*, 2014]. Seismic information on the central ∼500 km of the Moon is uncertain due to lack of seismic waves penetrating this region. The curious lack of farside moonquakes has long been considered to be an indication of an attenuating, possibly molten, region in the deep lunar interior [*Nakamura et al.*, 1973; *Nakamura*, 2005]. Recent analysis of the Apollo lunar seismic data for core-reflected phases has yielded tentative evidence for an outer molten and inner solid core [*Weber et al.*, 2011; *Garcia et al.*, 2011] that is possibly overlain by a partially molten layer [*Weber et al.*, 2011]. Other lines of evidence for a lunar core include analysis of Apollo era and more recent Lunar Prospector and Kaguya electromagnetic sounding data, which because of limited acquisition span, only place an upper bound on lunar core radius [e.g., *Hood et al.*, 1982; *Hobbs et al.*, 1983; *Hood et al.*, 1999; *Khan et al.*, 2006a; *Grimm and Delory*, 2012; *Shimizu et al.*, 2013]. For more details of lunar structure we refer to the reviews of *Wieczorek et al.* [2006], *Lognonné and Johnson* [2007], *Jaumann et al.* [2012], and *Khan et al.* [2013].

Additional constraints on the deep lunar interior derive from knowledge of present-day lunar thermal structure, which controls the dynamic behavior of the mantle, its internal physical state including crucial parameters such as elastic properties, tidal and seismic dissipation, and transport properties (e.g., viscosity, conductivity, and diffusivity). Using various approaches that rely on the temperature dependence of elastic and anelastic properties and electrical conductivity of mantle minerals several studies have provided estimates of the lunar geotherm [e.g., *Hood et al.*, 1982; *Khan et al.*, 2006a, 2006b; *Kuskov et al.*, 2002; *Kuskov and Kronrod*, 2009, 2014; *Nimmo et al.*, 2012; *Grimm*, 2013; *Karato*, 2013]. Distinguishing between melt-free [e.g., *Nimmo et al.*, 2012] and melt-containing [e.g., *Williams et al.*, 2001; *Khan et al.*, 2004] lunar models on the basis of these selenotherms, however, is not possible given that the uncertainty on temperature in the deep lunar interior is ±200–300°C [*Khan et al.*, 2006a, 2006b; *Kronrod and Kuskov*, 2011].

Given the uncertainty associated with the existence of a molten layer in the lunar interior, our purpose here is to combine geophysical inverse analysis with phase-equilibrium modeling, following the approach of *Khan et al.* [2007], to derive information about the thermochemical and physical structure of the Moon. More specifically, our intentions are (1) to assess whether a deep-seated molten layer is a geophysical requirement and (2) to determine composition, thermal state, and physical properties of the melt. For this purpose, we simultaneously invert a set of geophysical data that bear on the deep lunar interior: mean mass and moment of inertia, Love number, and electromagnetic sounding data. Combining these various data sets allows for improved sensitivity throughout the lunar interior. Although volatiles have been found in several lunar samples [e.g., *Saal et al.*, 2008; *Boyce et al.*, 2010; *Hauri et al.*, 2011; *Greenwood et al.*, 2011] and are suggested by petrological modeling studies [*Elkins-Tanton and Grove*, 2011], the bulk lunar volatile content is unknown but is probably low [*Hirschmann et al.*, 2012]. In this regard, it is remarked that the presence of hydroxylated apatite does not necessarily imply a wet lunar interior [*Tartése and Anand*, 2012]. In view of this situation we assume that the lunar interior is anhydrous.

## 2. Melt in the Deep Lunar Interior

As reviewed elsewhere in detail [e.g., *Khan et al.*, 2004] the existence of partial melt in the lunar interior was suggested based on signal characteristics of, at that time, the sole located farside deep moonquake and a distant meteoroid impact. Strong shear wave arrivals, the distinguishing sign of deep moonquakes, were only observed at the two closest stations corresponding to bottoming depths of ∼1100 km. Waves having bottomed deeper showed no prominent shear wave arrivals and were inferred to have been attenuated during the traverse of a partially molten region [*Nakamura et al.*, 1973]. *Nakamura et al.* [1974] also reported a farside meteorite impact that occurred almost diametrically opposite to the lunar seismic stations. Given the delayed *P* wave arrival associated with this peculiar event, the signal was interpreted to indicate a low-velocity central region; however, other interpretations of this event are possible [*Sellers*, 1992]. In the ∼8 years that the Apollo lunar seismic experiment was underway, more than 12,000 events were recorded of which ∼7000 have been classified as deep moonquakes through correlation of seismic waveforms [*Nakamura*, 2003, 2005]. Of all located deep moonquake clusters to date none occur within ∼40° of the antipode of the Moon [*Nakamura*, 2005]. This implies either that moonquakes are absent in this region or that seismic waves are attenuated upon traversing the central part due to presence of partial melt. For details on the lunar seismic experiment we refer to *Lognonné and Johnson* [2007], *Nakamura* [2010], and *Khan et al.* [2013].

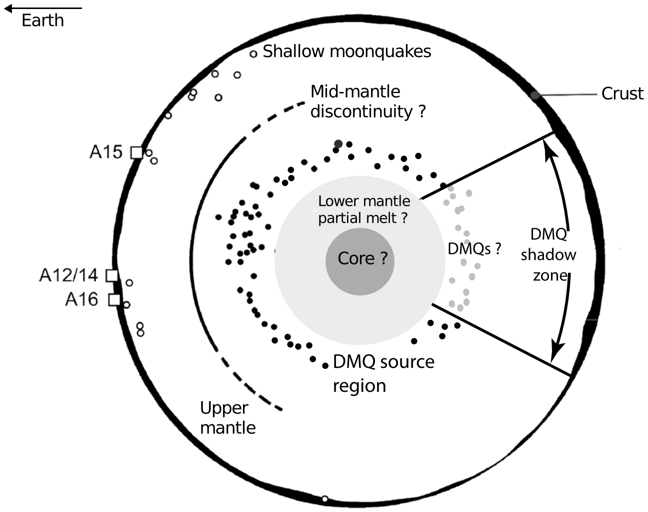

**Figure 1.** Schematic diagram of the gross internal structure of the Moon. A12–A16 indicate relative location of Apollo lunar seismic stations on the lunar nearside. Deep moonquakes are abbreviated as DMQs. Modified from *Wieczorek et al.* [2006]. See main text for details.

Recently, *Weber et al.* [2011] and *Garcia et al.* [2011, 2012] have reported observations of seismic phases that are purportedly core reflections. These phases, like many other later-arriving phases, are buried in the lunar seismic coda as a result of which they are difficult to extract. Although both the aforementioned studies rely on stacking of many deep moonquake waveforms to enhance the signals above the level of the coda, it is yet to be demonstrated that this method produces consistent results across all stations. As a consequence of the difficulties associated with this type of processing, the interpretation of the results by *Weber et al.* [2011] and *Garcia et al.* [2011] differs significantly. Garcia et al. favor a core with a radius of 380 ± 40 km with an outer liquid part (note that core shear wave speed is not determined), while *Weber et al.* [2011] find a 150 km thick partially molten mantle layer overlying a 330 km radius core, whose outer 90 km is liquid.

Analysis of recent magnetic field data acquired from the Kaguya satellite showed detection of a signal emanating from the lunar core as demonstrated by *Shimizu et al.* [2013]. Core size was estimated to be 290 km with an upper bound of 400 km. Additional analysis was carried out to study the influence of a partial melt layer at the bottom of the mantle on core size estimate. While it was found that a 150 km thick highly conductive partial melt layer would lead to an overestimation of core size of 40 km, it was acknowledged that the time span over which magnetic field data were analyzed was not long enough to robustly estimate any slowly varying field variations associated with a highly conductive partial melt layer.

Other geophysical evidence for a deep melt layer comes from analysis of more than 40 years of LLR data [e.g., *Williams et al.*, 2001, 2012]. Through the detection of a displacement of the Moon's pole of rotation, an indication that dissipation is acting on the rotation, *Williams et al.* [2001] found that only a combined dissipation due to monthly solid-body tides raised by the Earth and Sun and a fluid core with a rotation distinct from that of the solid body were able to account for the data. In an independent analysis of the solution parameters (tidal dissipation and Love number) determined by *Williams et al.* [2001], *Khan et al.* [2004, 2005] found evidence for the presence of a region in the deep lunar interior that was much less rigid (reduced shear modulus) than the solid mantle. The most plausible inference from this evidence is that a partially molten region encompasses the lunar core. Although a partially molten zone plausibly dominates tidal damping, LLR measurements are less sensitive to the exact location of a highly dissipative layer.

The case for partial melt at depth has been further strengthened in a very recent study by *Harada et al.* [2014] who numerically simulated the lunar viscoelastic tidal response. Based on the assumption of Maxwellian rheology, i.e., linear stress-strain relationship, *Harada et al.* [2014] find that the presence of a very low viscosity layer surrounding the core is able to explain tidal dissipation measurements at monthly and annual periods. An observation that more complex rheological models have been unable to account for [e.g., *Nimmo et al.*, 2012]. This low-viscosity layer is thought to act like a partially molten zone where most of the dissipation occurs.

In summary, geophysical evidence suggests the presence of a deep-seated lunar melt layer, although there is ambiguity as to whether the layer is located in the deep mantle or is part of the core (Figure 1).

Evidence provided by geochemical and petrological analyses of lunar rocks is more indirect. The chemical composition of a set of lunar volcanic rocks known as high-Ti basalts are characterized by high $TiO_2$ and FeO content [e.g., *Delano*, 1986]. The Ti content of these volcanic rocks is believed to be related to melting of

**Table 1.** Summary of Lunar Geophysical Data Parameters, Uncertainties, and Sources Used in the Inversion

| Data Parameter | Observed Value (± Uncertainty) | Source |
|---|---|---|
| Mean radius ($R$) | 1737.151 km | *Williams et al.* [2014] |
| Tidal Love number ($k_2$) | $0.02422 \pm 0.00022$ | *Williams et al.* [2014] |
| Tidal quality factor ($Q$) | $37.5 \pm 4$ | *Williams et al.* [2014] |
| Mean mass ($M$) | $7.3463 \pm 0.00088 \cdot 10^{22}$ kg | *Williams et al.* [2014] |
| Mean moment of inertia ($I/MR^2$) | $0.393112 \pm 0.000012$ | *Williams et al.* [2014] |

late-stage magma ocean cumulates that were enriched in ilmenite [e.g., *Taylor and Jakes*, 1974; *Hess*, 1991; *Snyder et al.*, 1992; *Wagner and Grove*, 1997; *Shearer and Papike*, 1999]. Toward the end of magma-ocean crystallization ilmenite-bearing cumulates would have formed a thin layer at the base of the crust and, owing to their high density relative to surrounding mantle, would become gravitationally unstable (cumulate pile overturn) and sink [e.g., *Hess and Parmentier*, 1995; *Shearer and Papike*, 1999; *Elkins-Tanton et al.*, 2002, 2011; *Shearer et al.*, 2006]. Moreover, as ilmenite cumulates likely also integrated heat-producing elements (U, Th, and K), they might be responsible for having initiated melting at depth [e.g., *Shearer et al.*, 1991] producing dynamically stable $TiO_2$-rich melts in the deep lunar interior [e.g., *Delano*, 1990; *Sakamaki et al.*, 2010; *van Kan Parker et al.*, 2012], providing an explanation for the presence of deep-seated partial melt [e.g., *Nakamura et al.*, 1973; *Williams et al.*, 2001; *Weber et al.*, 2011].

## 3. Data

The geophysical data that we consider here include mean mass ($M$) and moment of inertia ($I$), frequency-dependent electromagnetic sounding data (Apollo lunar dayside transfer functions), and second-degree tidal Love number ($k_2$). These data are sensitive to different physical properties (density, electrical conductivity, and shear modulus) and depth ranges ($M$, $I$, and $k_2$ sense integral properties), while depth sensitivity of transfer function data are frequency dependent and attain 1100–1300 km depth [e.g., *Hood et al.*, 1982; *Khan et al.*, 2006a]. Values adopted here for $M, I/MR^2$, and $k_2$ are summarized in Table 1 and are based on the most recent results obtained from the Gravity Recovery and Interior Laboratory (GRAIL) mission [*Williams et al.*, 2014].

Measured values for mean mass and moment of inertia are based on the value of *Williams et al.* [2014] and rescaled to a mean lunar radius $R$ of 1737.151 km. The value employed here for $k_2$ is obtained from analysis of GRAIL data and represents a weighted mean of independent determinations by *Konopliv et al.* [2013] and *Lemoine et al.* [2013] with an order-of-magnitude improvement in estimated uncertainty in comparison to the latest LLR determination [*Williams et al.*, 2014].

As the mantle of a planetary body is being deformed due to an external tide-raising potential, energy is dissipated within its interior. Dissipation of energy associated with anelastic properties of a planet is usually expressed as $1/Q$ where $Q$ is the quality factor. $1/Q$ is commonly defined as the ratio of energy dissipated to the peak energy stored in the system during a cycle such that low $Q$ values are representative of highly dissipative media [e.g., *Anderson*, 1989]. In this context, the inversion presented here is based on computing mantle properties in the elastic limit, i.e., in the infinite-frequency limit. In contrast hereto, the observed Love number $k_2$ is obtained at a frequency $\omega$ of the lunar tide ($\sim 4 \cdot 10^{-7}$ Hz), where anelastic effects are nonnegligible [e.g., *Nimmo et al.*, 2012; *Efroimsky*, 2012; *Williams et al.*, 2014]. This is summarized in the LLR-observed low $Q$ value of $37.5 \pm 4$ [*Williams et al.*, 2014], implying that a large amount of energy is currently being dissipated within the lunar interior [e.g., *Williams et al.*, 2001; *Khan et al.*, 2004; *Nimmo et al.*, 2012; *Efroimsky*, 2012; *Harada et al.*, 2014].

Therefore, prior to inversion, the observed tidal Love number should be corrected for anelastic contributions in order that it is representative of purely elastic effects. To this end, we follow the approach of *Zharkov and Gudkova* [2005], who adopt a Kelvin Earth model, i.e., an elastic incompressible homogeneous sphere, assumed to be valid in the seismic frequency range ($\omega_s$ ~1 Hz) and derive (see Appendix A for details) a correction at tidal frequencies $\omega_m$ to obtain

$$k_2(\omega_s) = \frac{k_2(\omega_m)}{1 + \frac{1}{Q(\omega_m)}\left[1 - \left(\frac{\omega_m}{\omega_s}\right)^{\alpha}\right] \cot \frac{\alpha\pi}{2}} \tag{1}$$

**Table 2.** Solution Notation, Formulae, and Model Sources[a]

| Symbol | Solution | Formula | Source |
|---|---|---|---|
| cpx | clinopyroxene | $CaMg_xFe_yCr_{1-x-y}Si_2O_6$, $x+y \leq 1$ | *Holland and Powell* [1996] and *Klemme et al.* [2009] |
| gt | garnet | $[Fe_xCa_yMg_{1-x-y}]_3[Cr_uAl_{1-u}]_2Si_3O_{12}$, $x+y \leq 1$ | *Holland and Powell* [1998] and *Klemme et al.* [2009] |
| ilm | ilmenite | $[Mg_xFe_{1-x}]_2TiO_3$ | ideal |
| melt | melt | Ca-Mg-Fe-Al-Ti-Cr-silicate melt | *Ghiorso et al.* [2002] |
| ol | olivine | $[Mg_xFe_{1-x}]_2SiO_4$ | *Holland and Powell* [1998] |
| opx | orthopyroxene | $[Mg_xFe_{1-x}][Cr_uAl_vMg_wFe_{1-u-v-w}]$ $[Cr_uAl_vSi_{1-u-v}]SiO_6$, $u+v+w \leq 1$ | *Holland and Powell* [1998] and *Klemme et al.* [2009] |
| sp | spinel | $Mg_xFe_{1-x}[Cr_uAl_{1-u}]_2O_3$ | *Holland and Powell* [1998] and *Klemme et al.* [2009] |

[a] Unless otherwise noted, the compositional variables $u, v, w, x$, and $y$ may vary between zero and unity and are determined as a function of the computational variables by free-energy minimization.

where the exponent $\alpha$ characterizes the frequency dependence of the dissipation. Based on seismic, geodetic, and laboratory studies $\alpha$ has been determined to be in the range 0.1–0.4 [e.g., *Anderson and Minster*, 1979; *Smith and Dahlen*, 1981; *Gribb and Cooper*, 1998; *Benjamin et al.*, 2006; *Jackson and Faul*, 2010]. For the inversions conducted here we employ a value of $\alpha$ of 0.3, which results in a purely elastic $k_2$ of 0.0232. Implications of the choice of $\alpha$ will be discussed further in section 7.1.1.

Finally, the lunar dayside transfer functions in the form of apparent resistivity $\rho_a(\omega)$ are measurements of the lunar inductive response to time-varying external magnetic fields during intervals when the Moon was in the solar wind or terrestrial magnetosheath [e.g., *Hood et al.*, 1982; *Sonett*, 1982]. The transfer function data are functions of frequency ($\omega$ denotes frequency) with longer periods sensing deeper and shorter periods shallower. The transfer function or apparent resistivity data are tabulated in *Hobbs et al.* [1983].

## 4. Petrological Modeling

The composition of the lunar mantle was explored within the system CaO-FeO-MgO-$Al_2O_3$-$SiO_2$-$TiO_2$. The mantle mineralogy is assumed to be dictated by equilibrium and is computed from thermodynamic data for a given model pressure, temperature, and bulk composition by Gibbs energy minimization [*Connolly*, 2005]. These calculations were made taking into consideration the stoichiometric solid phases and species in the thermodynamic data compilation of *Holland and Powell* [1998, revised 2002] together with the silicate melt and nonstoichiometric phases summarized in Table 2. The equilibrium assumption is dubious at low temperature [e.g., *Wood and Holloway*, 1984]. In recognition of this limitation, if a model required a mineralogy at a temperature below 800 K, then the equilibrium mineralogy was calculated at 800 K. Thermodynamic properties were then computed for the assemblage so obtained at the temperature of interest. The silicate melt model (pMELTS) [*Ghiorso et al.*, 2002] was originally calibrated using different thermodynamic data and models than used here. To minimize the inconsistency arising from this change, the reference state Gibbs energy and entropy of the pMELTS end-members were adjusted to match the liquidus temperatures and entropy changes for the end-members as reported by *Ghiorso et al.* [2002]. To test the resulting thermodynamic model, high-pressure liquidus phase relations were computed for the two synthetic picritic lunar glass compositions studied experimentally by *Elkins-Tanton et al.* [2003]. The model, extended to include $Cr_2O_3$ [*Klemme et al.*, 2009], reproduce the experimental phase relations reasonably well and, in particular, are in quantitatively good agreement with the pressure of the experimentally determined orthopyroxene-olivine cotectic. In contrast, the calculated liquidus temperatures are nearly 100 K higher than the experimental determination. While discrepancies of this magnitude are undesirable, they are not unexpected in light of the error analysis by *Ghiorso et al.* [2002], which suggests that the error in predicted liquidus temperatures rises from ∼50 K at 1 GPa to ∼200 K at 7 GPa. For present purposes, assuming the experimental determinations are correct, the error has the implication that our inverse modeling

**Table 3.** Olivine Conductivity Parameter Values [After *Yoshino et al.*, 2009]

| $\log_{10}(\sigma_i)$ | $H_i$ (eV) | $\log_{10}(\sigma_0^h)$ | $H_h$ (eV) | $\log_{10}(\sigma_0^p)$ | $H_0$ (eV) | $\beta$ |
|---|---|---|---|---|---|---|
| $4.73 \pm 0.53$ | $2.31 \pm 0.07$ | $2.98 \pm 0.85$ | $1.71 \pm 0.04$ | $1.9 \pm 0.44$ | $0.92 \pm 0.04$ | $0.16 \pm 0.02$ |

**Table 4.** Anorthite (An), Orthopyroxene (Opx), and Clinopyroxene (Cpx) Conductivity Parameter Values [After *Yang et al.*, 2011, 2012]

| Mineral | $\log_{10}(\sigma_h)$ | $H_h$ (kJ/mol) | $\log_{10}(\sigma_0^p)$ | $H_p$ (kJ/mol) | $r$ |
|---|---|---|---|---|---|
| an | $4.12 \pm 0.34$ | $161 \pm 6$ | $2.49 \pm 0.14$ | $77 \pm 2$ | $0.83 \pm 0.06$ |
| opx | $2.39 \pm 0.18$ | $105 \pm 3$ | $3.83 \pm 0.1$ | $81 \pm 1$ | $0.9 \pm 0.04$ |
| cpx | $2.16 \pm 0.27$ | $102 \pm 5$ | $3.56 \pm 0.1$ | $71 \pm 1$ | $1.13 \pm 0.05$ |

underestimates the amount of melt stable within the lunar mantle. Nonthermodynamic transport properties and aggregate elastic moduli were computed by averaging the Hashin-Shtrikman bounds.

## 5. Electrical Conductivity Data and Laboratory-Based Conductivity Profile

### 5.1. Mantle Mineral Electrical Conductivity Measurements

Experimental results show that electrical conductivity of minerals usually increase with temperature according to an Arrhenius relation [e.g., *Tyburczy and Fisler*, 1995]

$$\sigma = \sigma_0 \exp\left(-\frac{H}{kT}\right) \tag{2}$$

where $k$ is Boltzmann's constant, $T$ is absolute temperature, $\sigma_0$ is the so-called preexponential factor, and $H$ is activation enthalpy. The latter two parameters depend on the particular charge transport mechanism. Generally, conductivity of hydrous iron-bearing silicate minerals is given in terms of several charge transport mechanisms [e.g., *Yoshino*, 2010]

$$\sigma = \sigma_i + \sigma_h + \sigma_p \tag{3}$$

where $\sigma_i$, $\sigma_h$, and $\sigma_p$ denote contributions from ionic conduction (migration of Mg site vacancies), small polaron conduction (hopping of electrons between ferric and ferrous iron sites), and conduction arising from migration of protons, respectively.

Phases of present interest include anorthite (an), olivine (ol), orthopyroxene (opx), clinopyroxene (cpx), spinel (sp), garnet (gt), ilmenite (ilm), and melt. For hydroxylated olivine we employ the parameterization of *Yoshino et al.* [2009]

$$\sigma = \sigma_0^i \exp\left(-\frac{H_i}{kT}\right) + \sigma_0^h \exp\left(-\frac{H_h}{kT}\right) + \sigma_0^p C_w \exp\left(-\frac{H_0 - \beta C_w^{1/3}}{kT}\right) \tag{4}$$

where the different values of $\sigma_0$ and $H$ are preexponential factors and activation enthalpies for the various conduction mechanisms, respectively, $C_w$ is water content (note that since we make the assumption of an anhydrous lunar interior $C_w = 0$ here and in the following), and $\beta$ is a geometrical factor (Table 3). For anorthite, clinopyroxene, and orthopyroxene we rely on the measurements of *Yang et al.* [2011, 2012] and model conductivity for these minerals according to

$$\sigma = \sigma_0^h \exp\left(-\frac{H_h}{RT}\right) + \sigma_0^p C_w^r \exp\left(-\frac{H_p}{RT}\right), \tag{5}$$

where $R$ is the gas constant, $r$ is an exponent that determines the specific water dependence, and the remaining parameters are as delineated previously (Table 4). For garnet we consider the measurements by *Yoshino et al.* [2008] and use equation (2) to model conductivity (Table 5). For ilmenite we consider the measurements performed by *Katsura et al.* [2007] who found conductivity to vary according to

$$\sigma = \sigma_0 \exp\left(-\frac{E + PV}{kT}\right), \tag{6}$$

where $E$, $V$, and $P$ are activation energy, volume, and pressure, respectively (Table 6). No measurements are available for spinel; we disregard its contribution to conductivity in line with an earlier study [*Khan and Shankland*, 2012], where it was shown that omitting the contribution of a mineral that is present at levels

**Table 5.** Parameters Used to Characterize Conductivity of Garnet (gt)[a]

| Mineral | $\log_{10}(\sigma_0)$ | $H$ (eV) |
|---|---|---|
| gt (<1300 K) | 1.73 | 1.27 |
| gt (1300–1750 K) | 3.03 | 1.59 |
| gt (>1800 K) | 4.24 | 2.02 |

[a] For gt no uncertainties were provided in the original data [*Yoshino et al.*, 2008].

**Table 6.** Ilmenite (ilm) Conductivity Parameters [*Katsura et al.*, 2007]

| Mineral | $\sigma_0$ (S/m) | $E$ (eV) | $V$ (cm$^{-3}$/mol) |
|---|---|---|---|
| ilm | 15 ± 5 | 0.82 ± 0.06 | −1.5 ± 0.2 |

<10 vol % produces a difference in bulk conductivity of <0.02 log units. For melt conductivity we employ a physical parameterization as described in, e.g., *Khan and Shankland* [2012] and *Toffelmier and Tyburczy* [2007]. In this parameterization, we consider melt layer conductivity to vary from a "current" mantle value ($\sigma_m$) to some maximum (2 S/m + $\sigma_m$), where $\sigma_m$ is typically ≤1 S/m; see also section 6.4.4). Melt interconnectedness is important if melt conductivity is to dominate that of the resistive solid matrix [e.g., *Shankland and Waff*, 1977].

### 5.2. Bulk Electrical Conductivity Profile

Bulk electrical conductivity as a function of pressure (depth) for a given mineral assemblage (Figure 2) is obtained by combining the mineral phase proportions with the laboratory-measured mineral conductivities summarized above at the appropriate temperature, pressure, and composition. Contributions to bulk conductivity from single minerals are averaged using effective medium theory [*Landauer*, 1952; *Berryman*, 1995]. Use of this results in a self-consistent solution (an estimator, solid line in Figure 2) that has the important property of lying within the Hashin-Shtrikman bounds—the narrowest possible bounds that exist on an arbitrary multiphase system [*Hashin and Shtrikman*, 1962]. Details of this and other averaging schemes are described in, e.g., *Khan and Shankland* [2012] and *Xu et al.* [2000a].

### 5.3. Oxygen Fugacity and Miscellaneous Effects

Most of the experiments described above were carried out at oxygen fugacities ($f_{O_2}$) close to the Iron-Wuestite (IW) buffer. The experiments by *Yang et al.* [2011, 2012] were performed at $f_{O_2}$ controlled by the Ni-NiO buffer, while the measurements by *Yoshino et al.* [2008, 2009] were buffered by Mo-MoO$_2$, which is expected to be close to the IW buffer [*Longhi*, 1992], and *Katsura et al.* [2007] carried out their measurements at $f_{O_2}$ = IW. In comparison, the redox conditions of most lunar materials fall into the range ΔIW = −2 to ΔIW = 0 [*Sato et al.*, 1973; *Haggerty*, 1978]. This implies considerable overlap between lunar mantle redox conditions and those at which the experiments were performed obviating the need for $f_{O_2}$ corrections to electrical conductivity.

In relation to influence of oxygen fugacity, there has been some discussion in the literature [e.g., *Karato*, 2011; *Karato and Wang*, 2012] of the importance of correcting conductivity for $f_{O_2}$ in spite of the fact that these are not likely to exceed 0.5 log units and therefore a priori not geophysically discernable. *Karato* [2011], for example, considers an $f_{O_2}$ correction term to conductivity of the form

$$\sigma = \left(\frac{f_{O_2}}{f_{O_2}^{\mathrm{ref}}}\right)^q \sigma' \tag{7}$$

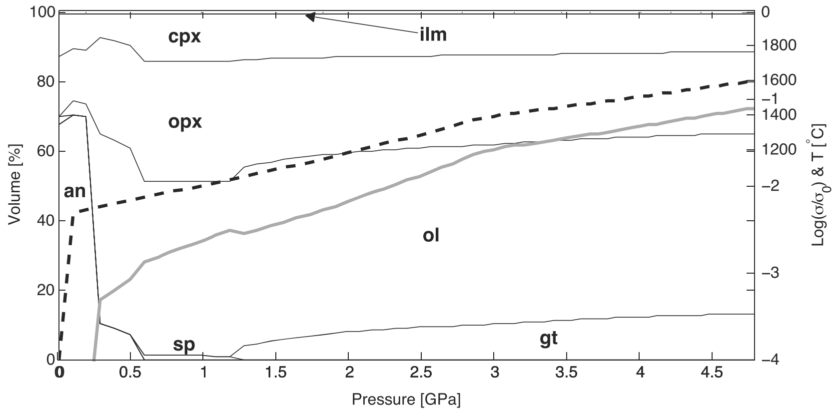

**Figure 2.** Variations in mineral phase proportions and laboratory-based bulk conductivity profile (gray line) computed for the anhydrous composition given in Table 8 (labeled "input") along a simple mantle adiabat (dashed line). Phases are anorthite (an), ol (olivine), opx (orthopyroxene), cpx (clinopyroxene), gt (garnet), spinel (sp), and ilmenite (ilm). See main text for further details. Mineral conductivities are summarized in Tables 3–6. $\sigma_0$ = 1 S/m.

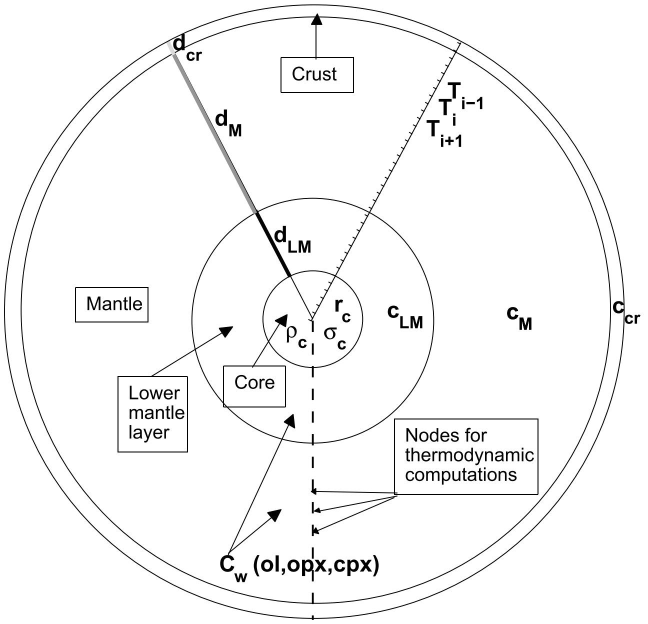

**Figure 3.** Model parameterization. The model is spherically symmetric, and model parameters are composition $c$ in the crust ($c_{\mathrm{cr}}$) and upper and lower mantle layers ($c_M$ and $c_{\mathrm{LM}}$), temperature $T$, thickness of crustal $d_{\mathrm{cr}}$ (fixed), upper mantle $d_M$ and lower mantle $d_{\mathrm{LM}}$ layers, core radius $r_c$, core conductivity $\sigma_c$, and core density $\rho_c$. For generality, we also included a set of parameters $C_W$ that describe the water content in major lunar mantle minerals. See main text for further details.

where $f_{O_2}$ is oxygen fugacity, $f_{O_2}^{\mathrm{ref}}$ is a reference conductivity, $q$ is an exponent, typically small (<1), that determines $f_{O_2}$ dependence (e.g., *Duba and Constable* [1993] and *Schock et al.* [1989] have determined $q$ for olivine and found a value of 1/6), and $\sigma'$ is conductivity prior to correction. In order to test the importance of oxygen fugacity effects on electrical conductivity via equation (7), we performed the same inversions (to be described) with the term added but found essentially no differences in comparison to inversions without this term. The reason for the absence of any significant effect is that the $f_{O_2}$ correction term advocated by Karato is not applied self-consistently, in the sense that $f_{O_2}$-related changes to phase equilibria are not considered concomitantly.

Apart from the activation volume for ilmenite, which is large and negative, we neglect the variation in conductivities due to pressure. This neglect is justified given (1) that pressure varies little over the depth of the lunar mantle and (2) that pressure effects on electrical conductivity of upper mantle minerals, particularly olivine, have been observed to be weak [*Xu et al.*, 2000b]. Conductivity of olivine, for example, was found to change by less than a factor of 2.5 when activation volume was varied $\pm 0.6$ cm$^3$/mol.

As in *Xu et al.* [2000a] and previous studies [e.g., *Khan and Shankland*, 2012] no corrections were made for grain boundary effects, given that substantial systematic variations in conductivity are yet to be observed [e.g., *Duba and Shankland*, 1982; *Roberts and Tyburczy*, 1993; *Xu et al.*, 2000a; *ten Grotenhuis et al.*, 2004; *Dai et al.*, 2008; *Watson et al.*, 2010].

Conductivity measurements performed by other groups, e.g., those by *Poe et al.* [2010] and *Wang et al.* [2006] on hydrous olivine, *Dai and Karato* [2009a, 2009b] and *Dai et al.* [2012] on hydrous orthopyroxene and pyrope-rich garnet, and *Romano et al.* [2006] on pyrope-almandine garnets were not considered here. For an alternative database containing these and other measurements the reader is referred to, e.g., *Pommier and Le Trong* [2011]. As discussed in detail in *Khan and Shankland* [2012] use of different data sets can result in different outcomes. However, as we consider uncertainties in measured conductivity parameters (see next section), we automatically provide for larger variations and are thus a priori less likely to bias the results.

$$\begin{tikzcd}
& & \mu,\kappa \arrow[r, "g_4"] & k_2 \\
c,T \arrow[r, "g_1"] & W \arrow[ur, "g_2"] \arrow[r, "g_2"] \arrow[dr, "g_3"] & \rho \arrow[r, "g_5"] \arrow[ur, "g_4"] & M,I \\
& & \sigma \arrow[r, "g_6"] & \rho_a(\omega)
\end{tikzcd}$$

**Figure 4.** A schematic illustration of the forward problem and the different model parameters ($c$ and $T$), physical theories ($g_1, g_2, \ldots, g_6$), secondary parameters ($W$, $\mu$, $\kappa$, $\rho$, and $\sigma$), and data ($k_2$, $M$, $I$, and $\rho$a) used to describe it. Symbols are described in section 3.2.

## 6. Computational Aspects

### 6.1. Parameterization

We assume a spherically symmetric model of the Moon (Figure 3), which is divided into a number of layers corresponding to crust, mantle, lower mantle layer, and core of which the latter three are variable in thickness. The crustal layer is parameterized using composition ($c_{\mathrm{cr}}$)

**Table 7.** Prior Bounds on Bulk Mantle Model Compositions (All Values in wt %)

| Component | Crust | Mantle |
|---|---|---|
| CaO | 13–18 | 1–8 |
| FeO | 5.5–7.5 | 5–15 |
| MgO | 6–8 | 25–55 |
| $Al_2O_3$ | 22–28 | 1–8 |
| $SiO_2$ | 40–50 | 35–55 |
| $TiO_2$ | 0.01–1 | 0.5–15 |

(see Table 7), temperature $T$ and fixed thickness $d_{cr}$. The mantle is divided into two layers that are parameterized by thicknesses $d_M$ and $d_{LM}$, composition $c_M$ and $c_{LM}$, and temperature $T$. Mantle compositions are uniform in each layer, and temperature is defined at a number of fixed radial nodes. The physical properties of the core are specified by radius ($r_c$), density ($\rho_c$), and electrical conductivity ($\sigma_c$). The core layer is simplified because we lack a thermodynamic database for modeling metallic compositions. To determine the mineralogical structure and corresponding mass density, it is also necessary to specify the pressure profile, which is obtained by integrating the load from the surface.

### 6.2. Forward Problem

The forward problem (Figure 4) consists of the following steps (all model parameters are assumed to be functions of radius):

Steps 1–2: $c, T \xrightarrow{g_1} W \xrightarrow{g_2} \mu, \kappa, \rho$. Equilibrium mineralogy $W$ and isotropic elastic parameters $\mu$ (shear modulus), $\kappa$ (bulk modulus), and density $\rho$ are computed using the thermodynamic code Perple_X [*Connolly*, 2005] (for details see section 4). Computed mineralogy for a given lunar composition and geotherm is illustrated in Figure 2.

Step 3: $W \xrightarrow{g_3} \sigma$. Computation of bulk electrical conductivity from laboratory estimates of single mineral conductivity is described in section 5.

Steps 4–6: $\mu, \kappa, \rho, \sigma \xrightarrow{g_4, g_5, g_6} k_2, M, I, \rho_a$. The final steps involve computing synthetic data that can be compared to observations. Computing Love numbers and transfer functions from radial profiles of $\mu, \kappa, \rho$, and $\sigma$ are described in *Khan et al.* [2004] and *Khan et al.* [2006b], respectively, and we refer to those studies for details.

### 6.3. Inverse Problem

Within a Bayesian framework, the solution to the general inverse problem $\mathbf{d} = g(\mathbf{m})$, where $\mathbf{d}$ is a data vector containing observations and g a typically nonlinear operator that maps a model parameter vector $\mathbf{m}$ into data, is given by [e.g., *Mosegaard and Tarantola*, 1995]

$$\sigma(\mathbf{m}) = kf(\mathbf{m})\mathcal{L}(\mathbf{m}), \tag{8}$$

where $k$ is a normalization constant, $f(\mathbf{m})$ is the prior probability distribution on model parameters (see next section), i.e., information about model parameters obtained independently of the data under consideration, $\mathcal{L}(\mathbf{m})$ is the likelihood function, which can be interpreted as a measure of misfit between the observations and the predictions from model $\mathbf{m}$, and $\sigma(\mathbf{m})$ is the posterior model parameter distribution containing the solution to the inverse problem. The particular form of $\mathcal{L}(\mathbf{m})$ is determined by the observations, their uncertainties, and how these are employed to model data noise (to be enunciated below).

To sample the posterior distribution (equation (8)) in the model space, we employ the Metropolis algorithm [e.g., *Mosegaard and Tarantola*, 1995]. Although this algorithm is based on random sampling of the model space, only models that result in a good data fit and are consistent with prior information are frequently sampled (importance sampling). The Metropolis algorithm is capable of sampling the model space with a sampling density proportional to the target posterior probability density without excessively sampling low-probability areas. This is particularly important when we consider high-dimensional model spaces in which a large proportion of the volume may have near-zero probability density.

### 6.4. Prior Information

#### 6.4.1. Crust and Mantle Composition

We model composition $c_k^i$ using the CaO-FeO-MgO-$Al_2O_3$-$SiO_2$-$TiO_2$ (CFMASTi) model system, where indices $i$ and $k$ run over crust or mantle layers and CFMASTi chemical components, respectively. Crustal and mantle compositions are varied uniformly within the bounds given in Table 7 with the constraint that a given composition sums to 100 wt % resulting in five independent chemical components that need to be determined in each layer. These wide ranges are chosen so as to encompass the entire suite of potential lunar compositions derived from sample, geochemical, and geophysical analyses [e.g., *Khan et al.*, 2006a; *Kuskov et al.*, 2002]. Results from the recent GRAIL mission have revealed that the density of the lunar highland crust is substantially lower than previously thought implying high levels of porosity that extend to a few kilometers depth [*Wieczorek et al.*, 2013; *Besserer et al.*, 2014]. To model effects of porosity on $\rho$, $P$ and $S$ wave speeds, we employ a simple function of the form $\rho_i' = \rho_i \cdot \phi$, where $\rho_i$ is density in crustal layer $i$ computed thermodynamically and $\phi$ is a porosity parameter that varies with depth based on the results from GRAIL [*Wieczorek et al.*, 2013]. This results in 18 compositional parameters.

### 6.4.2. Temperature

We assume mantle temperature to be uniformly distributed with no lower or upper bounds, except for a constant surface temperature of 0°C. We additionally employ the constraint $T_{j-1} \leq T_j \leq T_{j+1}$ where $T_j$ is temperature in layer $j$, i.e., temperature does not decrease with depth. In this scheme we determine temperature in 20 uniform layers, yielding 20 thermal parameters.

### 6.4.3. Layer Thickness

Crustal thickness is fixed at 40 km depth after *Wieczorek et al.* [2013], whereas thickness of the two mantle layers is variable via their interface. The latter is assumed to be uniformly distributed within the range 1100–1300 km depth; this yields one parameter.

### 6.4.4. Melt Layer Conductivity

Should a melt phase, for a given composition and geotherm, stabilize in the deep lunar interior, we consider, following *Khan and Shankland* [2012] and *Toffelmier and Tyburczy* [2007], melt layer conductivity to vary from the current"background" mantle value ($\sigma_m$), computed as described in section 4, and up to a maximum of $2 + \sigma_m$ (S/m), i.e., $\sigma_{\mathrm{melt}} = \sigma_m + 2\epsilon$, where $\epsilon$ is a randomly distributed number in the interval 0–1. These values are based on low-pressure conductivity measurements of various melts [e.g., *Pommier et al.*, 2010; *Yoshino et al.*, 2010].

### 6.4.5. Core

The core is parameterized in terms of radius ($r_{\mathrm{core}}$), density ($\rho_{\mathrm{core}}$), electrical conductivity ($\sigma_{\mathrm{core}}$), and shear ($\mu_{\mathrm{core}}$) and bulk ($\kappa_{\mathrm{core}}$) moduli. We assume $r_{\mathrm{core}}$ and $\rho_{\mathrm{core}}$ to be distributed uniformly in the intervals $0 < r_{\mathrm{core}} < 437$ km and $\rho_m < \rho_{\mathrm{core}} < \rho_c$, respectively, where $\rho_m$ is the value of $\rho$ at the base of the mantle and $\rho_c = 7.5$ g/cm$^3$ (density of pure $\gamma$-Fe at the conditions at the center of the Moon). Based on analyses of LLR data that appear to require the presence of a liquid core [e.g., *Williams et al.*, 2001, 2012], we fix $\mu_{\mathrm{core}}$ ~0 Pa (the value of $\kappa_{\mathrm{core}}$ is less important) throughout the core. This choice will be discussed further in section 7.1.1. $\sigma_{\mathrm{core}} \in [\sigma_m; \sigma_c]$, where $\sigma_m$ is electrical conductivity at the base of the mantle and $\sigma_c = 10^5$ S/m after *Stacey and Anderson* [2001].

### 6.4.6. Overall Parameterization

In summary, given values of the parameters described above we compute equilibrium modal mineralogy, density, bulk and shear moduli, and bulk conductivity from the surface downward as a function of pressure, temperature, and composition at intervals of 20 km in the depth range 1–1300 km providing adequate depth resolution.

The particular parameterization chosen here was found by conducting trial inversions and reflects a particular parameterization that is very near the simplest, while capable of fitting the data within uncertainties. Also, uncertainties on measured mineral physics parameters related to the thermodynamic formulation are presently not considered as we currently lack ability to model the various thermodynamic parameter trade-offs. As a result, actual uncertainties are likely larger than indicated here.

### 6.4.7. Electrical Conductivity Parameters

As in our previous analyses uncertainties in all parameters relevant to modeling conductivity (e.g., preexponential factor and activation enthalpy) are considered by assuming that these are uniformly distributed within bounds of $[p - \Delta p; p + \Delta p]$, where $p$ is any of the aforementioned parameters and $\Delta p$ the associated uncertainty.

## 6.5. Sampling the Posterior Distribution

We assume that data noise can be modeled using a Gaussian distribution and that observational uncertainties and calculation errors between the various data sets are independent. As a result the likelihood function can be written as

$$\mathcal{L}(\mathbf{m}) \propto \exp\left( -\frac{[d^M_{\mathrm{obs}} - d^M_{\mathrm{cal}}(\mathbf{m})]^2}{2\sigma^2_M} - \frac{[d^I_{\mathrm{obs}} - d^I_{\mathrm{cal}}(\mathbf{m})]^2}{2\sigma^2_I} - \frac{[d^{k_2}_{\mathrm{obs}} - d^{k_2}_{\mathrm{cal}}(\mathbf{m})]^2}{2\sigma^2_{k_2}} - \sum_{\omega} \frac{[d^{\rho_a(\omega)}_{\mathrm{obs}} - d^{\rho_a(\omega)}_{\mathrm{cal}}(\mathbf{m})]^2}{2\sigma^2_{\rho_a(\omega)}} \right) \quad (9)$$

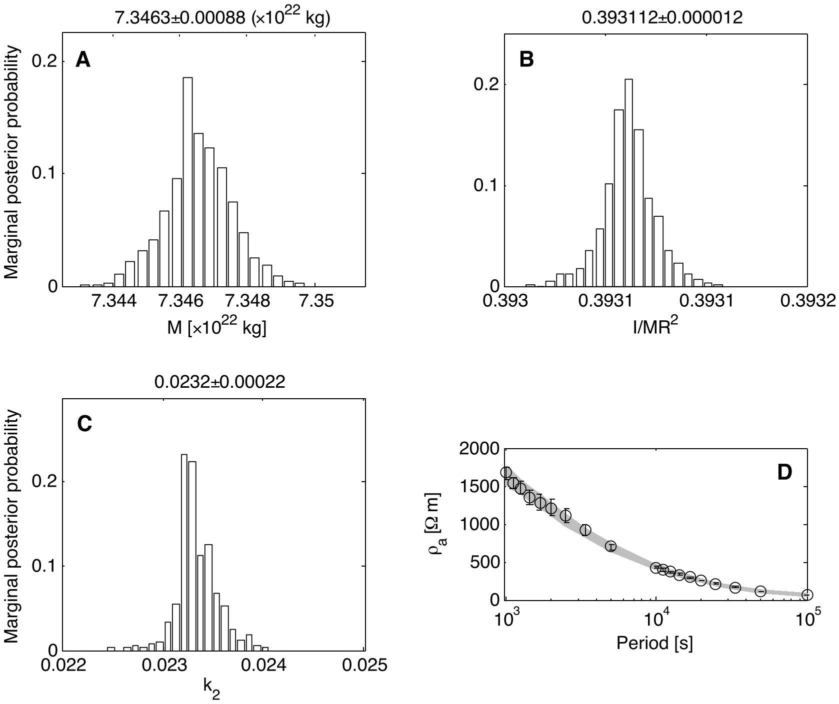

**Figure 5.** Computed data (synthetics). Data are computed from all sampled models retained for analysis here and include (a) mass, (b) moment of inertia, (c) $k_2$, and (d) electromagnetic sounding data. For the latter, observed lunar electromagnetic sounding data and error bars are superimposed, whereas observed values for mean mass, mean moment of inertia, and purely elastic $k_2$ are indicated above the histograms.

where $d_{\mathrm{obs}}$ denotes observed data, $d_{\mathrm{cal}}(\mathbf{m})$ calculated data, superscripts $M, I, k_2$, and $\rho_a(\omega)$ denote the various data sets, respectively, and $\sigma_M, \sigma_I, \sigma_{k_2}$, and $\sigma_{\rho_a(\omega)}$ uncertainty on either of these. $\rho_a(\omega)$ is apparent resistivity and a function of frequency $\omega$.

The main purpose of using a probabilistic inference approach to solving the nonlinear inverse problems posited here is not to present a single realization from the posterior distribution but to display the information gathered from a whole series of sampled models. A characteristic feature of this approach is that sampled models might be structurally different, thus accentuating diverse structural features within the Moon. However, and this is the important point, all models have relatively high likelihood values and fit data within uncertainties (see Figure 5). This implies that only the statistical nature of model features is of interest, which is analyzed and interpreted probabilistically. Note that in the following we limit ourselves to showing the posterior distributions only and omit, for brevity, the corresponding prior distributions.

## 7. Results and Discussion

### 7.1. Implications for Lunar Internal Structure

#### 7.1.1. A Partially Molten Interior: Seismic Structure

The presence of partial melt deep in the lunar mantle has been suggested as part of the interpretation of a seismically defined attenuating zone at the bottom of the mantle [e.g., 1973; *Nakamura*, 2005; *Weber et al.*, 2011]. Independent observations and analyses based on LLR data support this interpretation, although the distinction between this and a partially or entirely molten core has been less clear [e.g., *Williams et al.*, 2001, 2012; *Khan et al.*, 2004; *Khan and Mosegaard*, 2005]. Our inversion results are shown in Figure 6 (all illustrated models fit data within uncertainties) and indicate that the deep lunar interior is partially molten. In particular, shear wave speed profiles clearly point to the presence of significant amounts of melt at depths ≥1200 km that reach values as low as ~1 km/s. This melt zone effectively comprises about 100–150 km of the bottom mantle (depth range ~1250–1400 km) where temperatures in excess of 1600°C are reached (see section 7.1.3 for further discussion). The present result is in good agreement with that of *Harada et al.* [2014], who found evidence for a low-viscosity layer at the bottom of the mantle (depth range ~1250–1400 km) from viscoelastic tidal dissipation modeling. This low-viscosity layer is interpreted to represent a partially

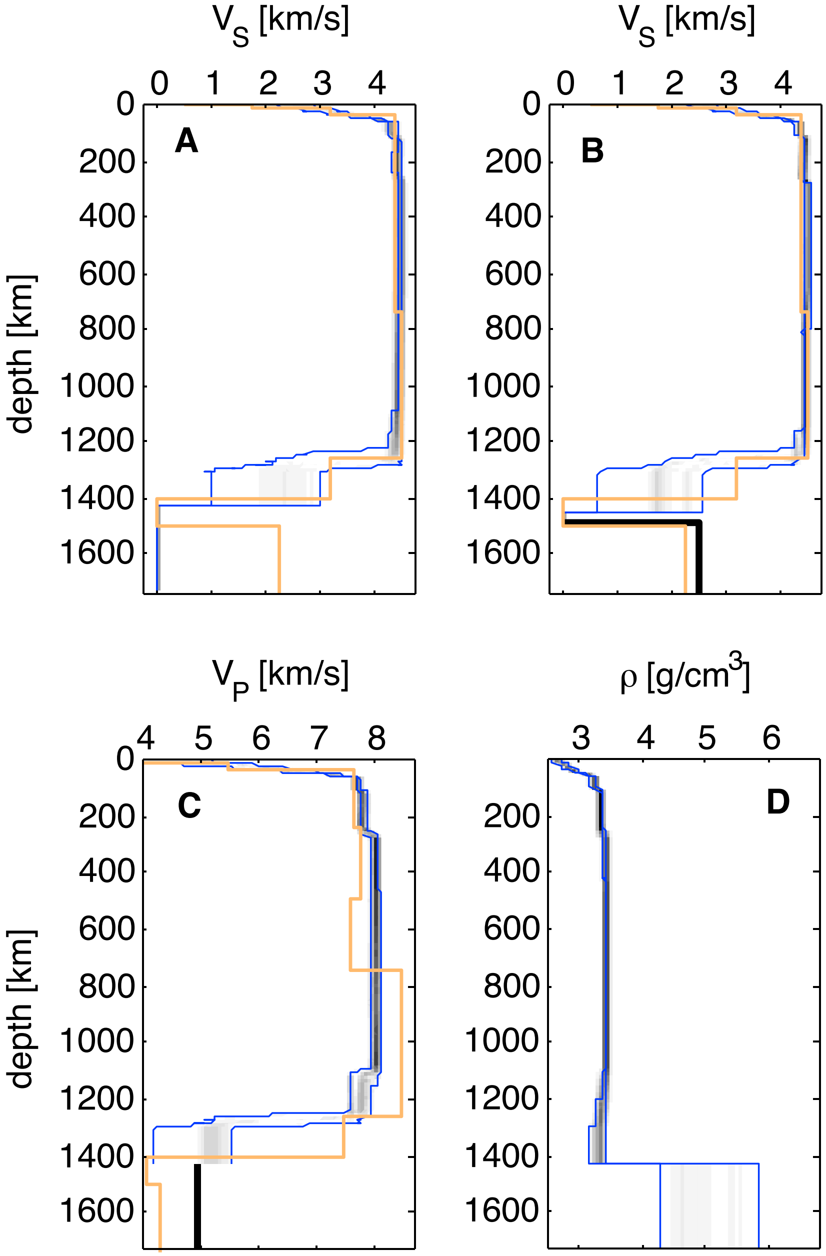

**Figure 6.** Inverted mantle physical properties: (a and b) *S* wave speed, (c) *P* wave speed, and (d) density. Sampled models are shown as regions of probability, with black and white colors indicating high and low probability of occurrence, respectively. Difference between Figures 6a and 6b is due to different assumptions of physical properties of the inner core: liquid (Figure 6a) and solid (Figure 6b). The *P* wave speed and density profiles shown correspond to the *S* wave speed models shown in Figure 6a. In Figures 6a–6c the light brown line shows the seismic wave speed model from *Weber et al.* [2011]. Note that *Weber et al.* (2011) only determined melt-layer and core properties (seismic wave-speeds and extent/size). The models for the mantle and crust were taken from *Gagnepain-Beyneix et al.* (2006). Also, no density model was determined. In all plots blue lines indicate the 95% upper and lower credible intervals. Models derived here will be available from http://jupiter.ethz.ch/~akhan/amir/Home.html.

molten region surrounding a liquid core, although *Harada et al.* [2014] did not attempt to independently determine elastic structure of the mantle and core but only rheology and outer radius of the low-viscosity layer. Their background structure was based on the model of *Weber et al.* [2011]. Undoubtedly, other models possibly exist that fit data, but the importance of their low-viscosity partial melt layer model is its ability to match the observed lunar tidal quality factor *Q* at (1) both monthly and annual periods and (2) the weak negative frequency dependence of $Q$ that results in a decrease of $Q$ with increasing frequency as observed from analysis of LLR data [e.g., *Williams et al.*, 2001].

As noted in section 6.4 we fix core state to be entirely liquid in line with inferences drawn from LLR data [e.g., *Williams et al.*, 2001]. To test the implications of this for the melt layer, we performed a set of additional inversions where we assumed the inner core to be solid and the outer core to be liquid in line with the model proposed by *Weber et al.* [2011]. Inner core radius was fixed to 250 km because of lack of data sensitivity to this parameter, while outer core radius figured, as before, as a model parameter. Inner core shear wave speed was fixed to 2.5 km/s [cf. *Weber et al.*, 2011]. The results of these inversions are also shown in Figure 6 and clearly support the contention of a deep lunar melt layer. Small differences are palpable; the melt layer appears to be slightly thicker (10–20 km) and also seems to sample slightly lower shear wave speeds (down to ∼0.5 km/s) than in the liquid core case.

For comparison, the seismic shear wave speed model of *Weber et al.* [2011] is also shown. The approximate location and size of the partial melt zone is observed to agree fairly well with the determination here, whereas absolute $P$ and $S$ wave speeds within the melt layer appear to be overestimated by *Weber et al.* [2011]. Several factors come into play here. First of all, discrepancies have to be viewed in the light of the limiting resolution and poor sensitivity to overall core properties that exists in the approaches of *Weber et al.* [2011] and *Garcia et al.* [2011] as discussed in section 2. Second, and in addition to poor resolution, absolute velocities in the core trade off with those in the mantle, which can significantly influence estimated core properties. This is accentuated in the difference between the core models of Weber et al. and Garcia et al. Third, whereas Garcia et al. determine mantle seismic wave speed structure in addition to core properties (only density and radius), Weber et al. do not independently attempt to retrieve mantle structure but instead fix mantle wave speeds and densities to the model of *Gagnepain-Beyneix et al.* [2006]. As a consequence, different mantle structures may provide the explanation for the differences in the core models of Weber et al. and Garcia et al. and the models obtained here. Note also that while no uncertainty estimates are quoted for the mantle model of Weber et al., these are in the range ∼0.3–1 km/s depending on depth [*Gagnepain-Beyneix et al.*, 2006]. Also, No uncertainties are quoted for core properties.

As a point of observation, we would like to note that the tidal Love number reported by *Weber et al.* [2011] for the model including a partially molten layer in the depth range ∼1250–1400 km is 0.0232, which is in close agreement with our anelastically corrected $k_2$ value. For comparison, in the inversion of *Garcia et al.* [2011], where no partially molten layer was found, much lower $k_2$ values ($0.0213 \pm 0.0025$) were considered that correspond to solid-body values. To reduce rigidity, small amounts of melt or liquid have to be present in the deep lunar interior and several numerical simulations and inversions have shown that $k_2$ correlates positively with melt vol %. These results thus support the observation that lunar rigidity decreases significantly in the deep mantle (Figure 6) and suggests that a dissipative region, such as a partially molten layer, is required at the depth of the core-mantle boundary to fit the observed Love number in accordance with LLR-based observations and viscoelastic modeling [e.g., *Williams et al.*, 2001; *Harada et al.*, 2014].

Additional melt-free runs where data sets/points were inverted separately clearly showed the sensitivity of $k_2$ to rigidity structure of the deep lunar interior. The other data sets all fit observations within uncertainties, except for $k_2$. This indicates, as expected, that the data point most sensitive to the melt zone is $k_2$. However, the importance of considering the other data jointly with $k_2$ is that these provide information about other parts of the model (cf. Figure 4) and thereby help constrain the part sensed mainly by $k_2$.

#### 7.1.2. A Partially Molten Interior: Dependence on $\alpha$

In correcting $k_2$ for the anelastic contribution (section 3), we assumed that dissipation is frequency dependent ($Q \propto \omega^{\alpha}$) with frequency exponent $\alpha$ as implied by the absorption band model of *Anderson and Minster* [1979]. As a result of the anelastic correction employed here both $k_2$ and $Q$ depend on frequency in agreement with predictions based on viscoelastic models [e.g., *Nimmo et al.*, 2012; *Efroimsky*, 2012; *Harada et al.*, 2014]. The value of $\alpha$, however, is less well determined, ranging from 0.1 to 0.4, based on seismic, geodetic measurements, and laboratory studies [e.g., *Anderson*, 1989; *Jackson et al.*, 2002; *Benjamin et al.*, 2006; *Nimmo et al.*, 2012]. To study the influence of $\alpha$ on the presence of a deep melt layer, we conducted inversions for several values of $\alpha$ in the range 0.1–0.4. We observed, as expected from the discussion in the previous section, that by lowering $\alpha$ (smaller $k_2$) the requirement for melting in the deep lunar interior disappears. While continuously diminishing in thickness as $\alpha$ decreases to 0.1, the melt layer disappears for $\alpha < 0.1$, approaching a solid-body $k_2$ value.

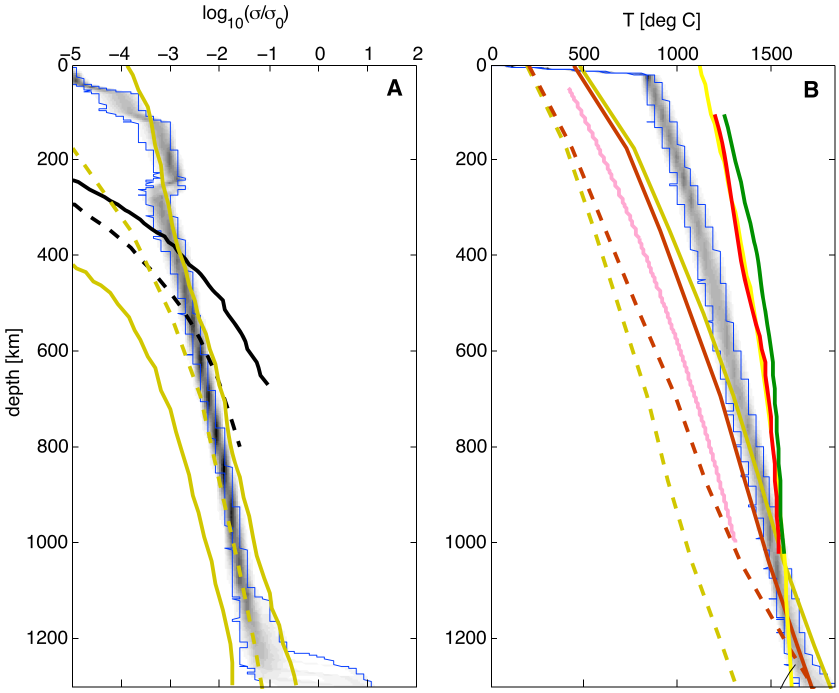

**Figure 7.** Mantle electrical conductivity and thermal structure. Plots show inverted (a) mantle bulk electrical conductivity ($\sigma_o$ = 1 S/m) and (b) temperature in the lunar interior. In Figure 7a yellow bold lines describe the range of conductivities determined by *Hood et al.* [1982] and black bold solid and dashed lines show two conductivity profiles taken from the study of *Grimm* [2013] that vary with Mg# (solid line: Mg# 75; dashed line: Mg# 85). The yellow dashed line is the conductivity profile considered by *Karato* [2013]. In Figure 7b temperature profiles from two other lunar geophysical studies have been included. The profiles from *Karato* [2013] are derived by assuming that the lunar mantle consists either of dry olivine (solid orange line), dry orthopyroxene (solid brown line), olivine containing 0.01 wt % $H_2O$ (dashed orange line), or orthopyroxene with 0.01 wt % $H_2O$ (dashed brown line). The pink solid line depicts the lunar mantle geotherm from *Kuskov and Kronrod* [2009]. Red, green, and yellow lines show the solidi of *Longhi* [2006] for the lunar primitive upper mantle (red) and Taylor Whole Moon (green) compositions and *Hirschmann* [2000] for peridotite (yellow), respectively. Blue lines in Figures 7a and 7b indicate 95% upper and lower credible intervals.

As noted earlier LLR is sensitive to tidal dissipation and when fitting LLR data *Williams et al.* [2001] detected four dissipation terms. A model that combined dissipation from tides and a fluid core was found to account for all four amplitudes (at periods of 1 month, 206 days, 1 year, and 1095 days). While dissipation at 1 month and 1 year could be fit with values of $\alpha$ that ranged from small positive to negative values, the 1095 day dissipation term could only be fit using negative exponents ($\alpha = -0.17 \pm 0.10$). This contrasts with observations from experimental, seismological, and geodetic measurements that point to positive values of $\alpha$ as expected for solid bodies such as Earth. A means of explaining this discrepancy would be to call for a more complex description where $\alpha$ depends not only on depth but also on rheological properties. Although speculative, there is some indication from data that appear to support such a model. First off, since dissipation is frequency dependent, we would expect that sensitivity in depth grows with increasing period [e.g., *Benjamin et al.*, 2006]. Thus, dissipation at relatively short-to-medium periods ($\leq$1 year) sounds the solid part of the upper and middle mantle and concurs with generally positive values of $\alpha$. Dissipation at longer periods (>1 year), on the other hand, probes the deeper mantle and core [e.g., *Benjamin et al.*, 2006], i.e., partial melt layer and liquid core. Since these parts behave rheologically differently than solid rock, a different value of $\alpha$ is not entirely unexpected. *Jackson et al.* [2004], for example, have found evidence that presence of melt can lead to a reduction of $\alpha$ in addition to a change of its sign in line with the LLR observations of *Williams et al.* [2001]. For the short periods considered in our study and because dissipation is not considered in detail, positive depth-independent values of $\alpha$ are a reasonable approximation. We leave it for future studies to consider this in more detail.

### 7.1.3. A Partially Molten Interior: Mantle Temperature and Conductivity Structure

Sampled lunar mantle temperature and bulk electrical conductivity profiles are shown in Figure 7. Average thermal gradients in the mantle range from 0.5 to 0.6°C/km, corresponding to temperatures around

**Table 8.** Literature, Input, and Inverted Model Compositions[a]

| Element | Crust (Input) | Bulk Mantle (Inverted) | Partial Melt (Inverted) | TWM | LPUM | KK11 |
|---|---|---|---|---|---|---|
| CaO | 16 | 2–6 | 4–8 | 4.6 | 3.18 | 3–4.7 |
| FeO | 6.5 | 10–13 | 14–24 | 10.9 | 7.62 | 9.9–12.1 |
| MgO | 7 | 32-36 | 29–32 | 32.7 | 38.3 | 29.5–38.8 |
| $Al_2O_3$ | 25 | 2–4.5 | 0–2 | 6.14 | 3.93 | 3.8–5.8 |
| $SiO_2$ | 45 | 40–46 | 36–40 | 44.4 | 46.1 | 49–52.3 |
| $TiO_2$ | 0.5 | 0.1–3 | 7–13 | 0.31 | 0.17 | – |

[a] As starting (input) mantle compositions we use the Taylor whole mantle composition [*Taylor*, 1982]. The crustal input composition is also taken from *Taylor* [1982]. LPUM and KK11 represent the lunar primitive upper mantle composition of *Longhi* [2003] and the average range in bulk mantle composition from different models as summarized by *Kronrod and Kuskov* [2011]. Inverted compositions quoted here correspond to the range containing the highest posterior probability. All numbers are in wt %.

1600–1800°C at 1300 km depth inside the partial melt layer. For reference, the lunar and peridotite solidi of *Longhi* [2006] and *Hirschmann* [2000] are also shown. The lunar solidi correspond to lunar primitive upper mantle (LPUM) [*Longhi*, 2003] and Taylor whole Moon (TWM) [*Taylor*, 1982] compositions (see Table 8). There is considerable overlap between the peridotite and LPUM solidi, reflecting similarity in composition. Moreover, we observe significant overlap between the location where melting is observed to occur presently and the location where the inverted lunar geotherms cross the solidi (below ∼1100 km depth). This suggests that melting is likely to occur in the deep lunar interior forming a highly dissipative layer that surrounds a possibly liquid core in line with the results presented in section 7.1.1.

The lunar conductivity profile shows, apart from a decrease below 200 km depth, a continuous increase in conductivity throughout the mantle. The negative conductivity gradient below 200 km depth is related to the increase in the fraction of olivine at the expense of orthopyroxene, which is more conductive than olivine. As expected the melt zone appears to comprise relatively high conductivities on account of the presence of melt, despite the limited sensitivity of the lunar dayside transfer functions to deep mantle structure.

In relation to lunar temperature and conductivity profiles estimated here, independent thermal models have been derived by *Kuskov and Kronrod* [2009], *Grimm* [2013], and *Karato* [2013], which are also shown in Figure 7, in addition to the Apollo era conductivity models of *Hood et al.* [1982]. The thermal profile obtained by *Kuskov and Kronrod* [2009] derives from mapping various Apollo era and more recent lunar seismic models into temperature. For this purpose Kuskov and Kronrod consider a number of compositions ranging from olivine pyroxenite over pyrolite to a Ca- and Al-enriched composition. Based on a thermodynamic modeling scheme in line with our implementation, Kuskov and Kronrod predict a range of mantle temperatures that result in seismic wave speeds that fit the literature models. The model shown in Figure 7 is summarized as approximating these results, and although no error bounds are provided, these are likely to be 200–400°C [see *Kuskov and Kronrod*, 2009, Figure 5]. Note that the model of Kuskov and Kronrod is only valid for subsolidus conditions, which provides part of the reason for the observed differences between the lunar geotherms, in addition to those related to differences in data.

The study of *Grimm* [2013] focuses on thermal evolution of the Procellarum KREEP Terrane and models this using a thermal conduction model that includes a range of thermal conductivities, heat production rates, KREEP layer thicknesses, and mantle starting temperatures. Importantly, Grimm couples these models with present-day estimates of topography, gravity, and electrical conductivity across the region. The results indicate that in order for the conductivity data (lunar transfer functions of *Hobbs et al.* [1983]) to be fit with purely conductive thermal profiles, the upper mantle needs to be compositionally enriched in either Fe or Al or contain an additional complement of water (hydrogen). Grimm favors Fe, corresponding to an upper mantle magnesium number of 75–80 (Figure 7), because of consistency with compositional estimates from combined thermochemical and seismic modeling [e.g., *Kuskov and Kronrod*, 2009; *Khan et al.*, 2006b] and thus with the results obtained here.

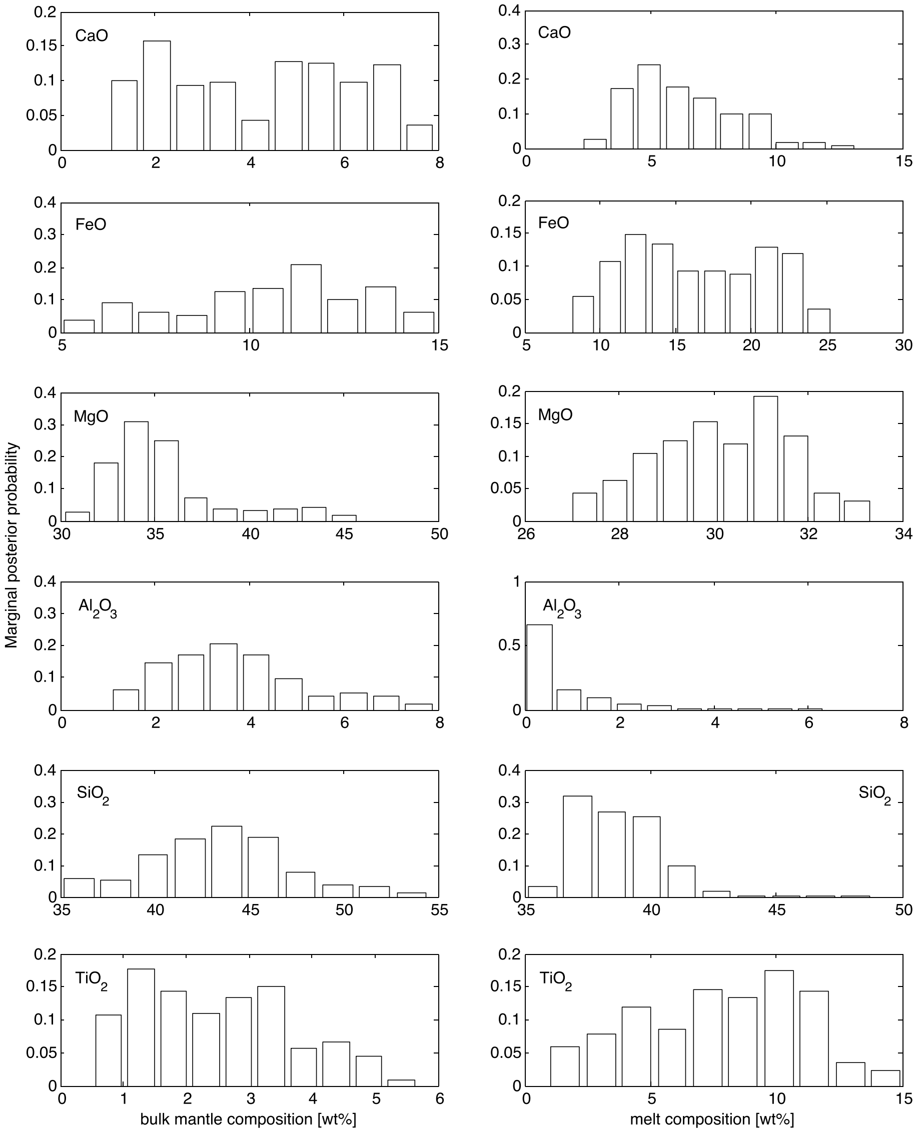

**Figure 8.** Sampled melt compositions for the neutrally to negatively buoyant models (cf. gray circles in Figure 9). Left and right columns show bulk mantle and melt compositions in the CFMASTi system (comprising the oxides of the elements CaO-FeO-MgO-$Al_2O_3$-$SiO_2$-$TiO_2$, respectively.

In the study of *Karato* [2013] a slightly different approach is taken. Karato considers the mean Apollo era conductivity profile derived by *Hood et al.* [1982] (dashed line in Figure 7A), in combination with the observed amount of tidal dissipation (*Q*) to simultaneously constrain the distribution of water and temperature in the mantle. Models are constructed on the basis of laboratory data and supplemented with theoretical models of the effect of water on conductivity and dissipative (anelastic) properties of the mantle. Based on various combinations of thermal profiles, water contents, and mantle mineralogy (either pure olivine or orthopyroxene), Karato concludes that (1) the lunar mantle appears to be cooler than Earth's (over the same pressure range), (2) to contain a similar complement of water as Earth's asthenosphere (∼0.01 wt %), and (3) is unlikely to be partially molten.

The latter conclusion contrasts with our observations and those of *Harada et al.* [2014] that seem to require the presence of melt in the deep lunar interior to explain the amplitude and frequency dependence of the observed tidal deformation. The observed discrepancy between Karato's model geotherms and ours is essentially due to adherence to dry conditions here. Additions of small amounts of water will indeed act to reduce temperatures in the mantle but will also lower the solidus [e.g., *Hirschmann*, 2006]. However,

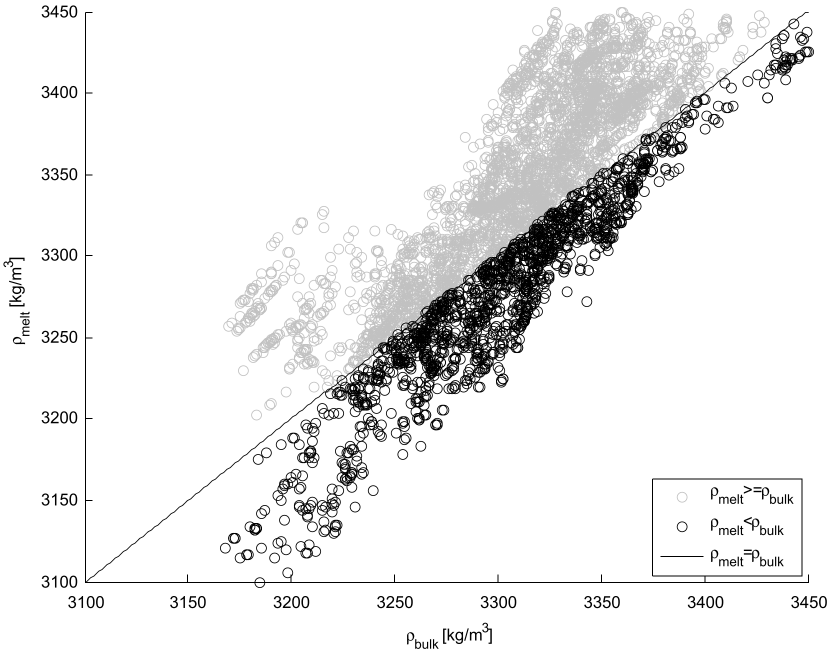

**Figure 9.** Melt density ($\rho_{melt}$) versus bulk density ($\rho_{bulk}$). Negatively buoyant models (gray circles) are located above the neutral buoyancy line (thin black line), while positively buoyant models (black circles) are located below.

estimating the latter effect quantitatively is complicated in the light of the unknown lunar mantle water content. Also, it should be kept in mind that the approach of *Karato* [2013], although very comprehensive, is nonetheless limited to "forward modeling" of a few models and comparison to literature estimates (conductivity profile), which can tend to obscure trade-offs between various model parameters (e.g., water content, $f_{O_2}$, temperature, composition, and mineralogy). In relation to the lunar conductivity model considered by *Karato* [2013], it appears that this particular conductivity profile is too resistive in the shallow lunar mantle and may not fit the lunar electromagnetic transfer function data (S.-I. Karato, personal communication, 2014). This evidently affects the modeled temperature profile and explains the offset between the thermal structure derived here and by *Karato* [2013] in the upper 600 km of the lunar mantle. In contrast to the upper mantle, the lower mantle (> 800 km depth) conductivity profile modeled by *Karato* [2013] coincides with the profiles derived here, as a result of which we observe considerable overlap between Karato's "dry" model geotherms and ours from ~800 km depth.

### 7.2. Melt Composition and the Fate of Ti-Rich Cumulates: Implications for Lunar Evolution

Bulk mantle and neutrally to negatively buoyant melt compositions derived here are shown in Figure 8 and summarized in Table 8. Bulk mantle compositions are generally found to agree with independent geophysical and cosmochemical estimates of lunar bulk silicate composition [e.g., *Warren*, 2005; *Taylor et al.*, 2006; *Kronrod and Kuskov*, 2011; *Taylor*, 2014]. With the exception of bulk mantle CaO and $TiO_2$ content, most of the elements appear to be well resolved. Another robust feature of the inverted compositions is the relative distribution of elements between bulk mantle and lower mantle melt layer. Melt composition will be discussed further below.

Melt density is critical through buoyancy. Our results show (see Figure 9) that melt density ranges from ~3.25 to 3.45 g/cm$^3$ at the core-mantle boundary (CMB), equivalent to pressures of ~4.5–4.6 GPa. Here we find that the largest concentration of gravitationally stable melts are centered in the density range 3.25–3.45 g/cm$^3$ with the largest number of models confined to the range 3.3–3.45 g/cm$^3$, whereas positively buoyant melts appear to be less common and span a narrower range ~3.2–3.35 g/cm$^3$.

The neutrally buoyant melt compositions (Figure 8) are observed to be strongly enriched (by factor of almost 2) in FeO and $TiO_2$ relative to bulk mantle. In comparison, the $TiO_2$ content of the picritic lunar glasses varies from 0.26 to 16.4 wt % [*Delano*, 1986]. According to various density studies [*Delano*, 1990; *Sakamaki et al.*, 2010; *van Kan Parker et al.*, 2011], our computed melt chemical compositions and

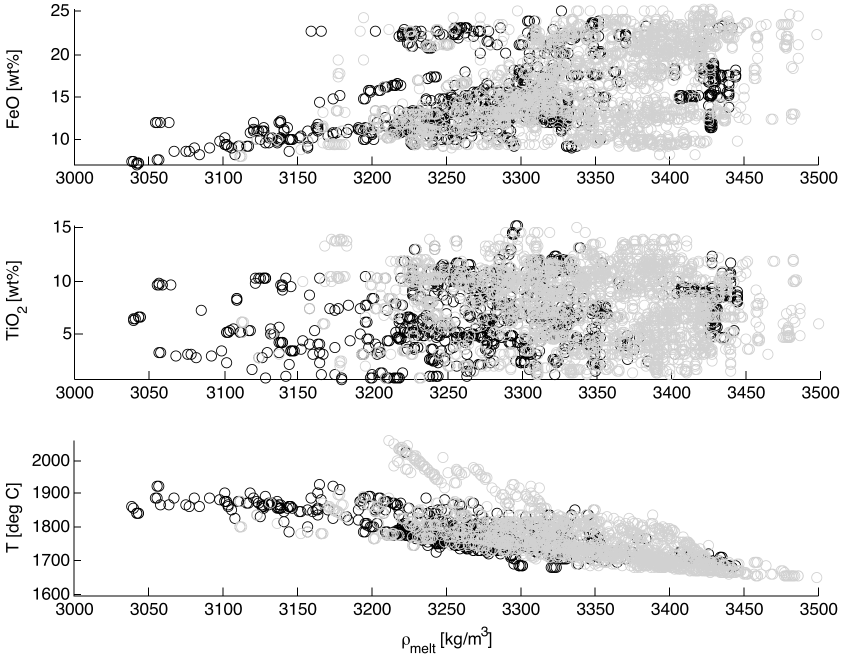

**Figure 10.** Compositional and thermal dependence of melt density. Gray and black circles indicate as in Figure 9 neutrally and positively buoyant models, respectively.

density values are in overall agreement with the melts that originated the green and orange glasses. These melts have low-to-moderate $TiO_2$ contents (≤9 wt % $TiO_2$) and are denser than mare basalts ($\rho$ <3.0 g/cm$^3$) but less dense than the Ti-rich melts that produced black glasses ($\rho$ >3.4 g/cm$^3$ at the CMB). However, we do not seek to match the lunar picritic glass compositions because the melt compositions obtained in the inversion are in equilibrium with the mantle host rocks, whereas the melts represented by lunar glasses were almost certainly modified during ascent through the mantle. Even if melt density is highly dependent on $TiO_2$ content [*Delano*, 1990], the models that produce neutrally buoyant melt are observed to have high FeO contents relative to the surrounding mantle and are not necessarily those with high $TiO_2$ contents. Figure 10 depicts variation in melt density as a function of composition (here limited to FeO and $TiO_2$) and temperature. While a positive correlation between melt density and FeO content is evident, no clear correlation is apparent in the case of $TiO_2$. Melt density is seen to decrease with increasing temperatures as expected.

The solid matrix of the partially molten layer (Figure 11) is typically garnet (if $\rho_{bulk} > \rho_{melt}$) or a mixture of garnet, olivine and orthopyroxene (if $\rho_{melt} > \rho_{bulk}$). In both cases, the computed proportion of melt that can be in equilibrium at the prevailing pressure and temperature conditions of the deep lunar interior is relative large (<40 vol %). For comparison, *Delano* [1990] has previously suggested that the proportion of melt in this layer cannot exceed 10 vol %, considering that sunk melts are Ti rich (20 wt %) and that the bulk abundance of $TiO_2$ in the Moon is 0.15–0.20 wt % [*Jones and Delano*, 1989].

*van Kan Parker et al.* [2011] demonstrated experimentally that molten orange glass will be less dense than equilibrium olivine. These authors also showed that the density crossover of the melt source of orange glass composition with orthopyroxene occurs at ~2.8 GPa (~520 km depth), meaning that these melts are buoyant with respect to their source region to 520 km depth, enabling their rise to the surface without external driving forces. Therefore, if melt with a density similar to the one investigated by *van Kan Parker et al.* [2011] is stored at the CMB, i.e., at a deeper depth than the density crossover, then the buoyancy of the melt could hinder its extraction to shallower depths and its involvement as part of lunar primary magma formation. This is in agreement with recent experimental results showing that only much denser melts (containing ~16 wt % $TiO_2$) are neutrally buoyant at the lunar CMB [*Sakamaki et al.*, 2010; *van Kan Parker et al.*, 2011].

The present-day temperatures that we find (cf. Figure 7) at a depth of 1200 km are ≥1600°C and thus in excess of the solidus temperatures (~1500°C) required for partial melting of $TiO_2$-rich material at high

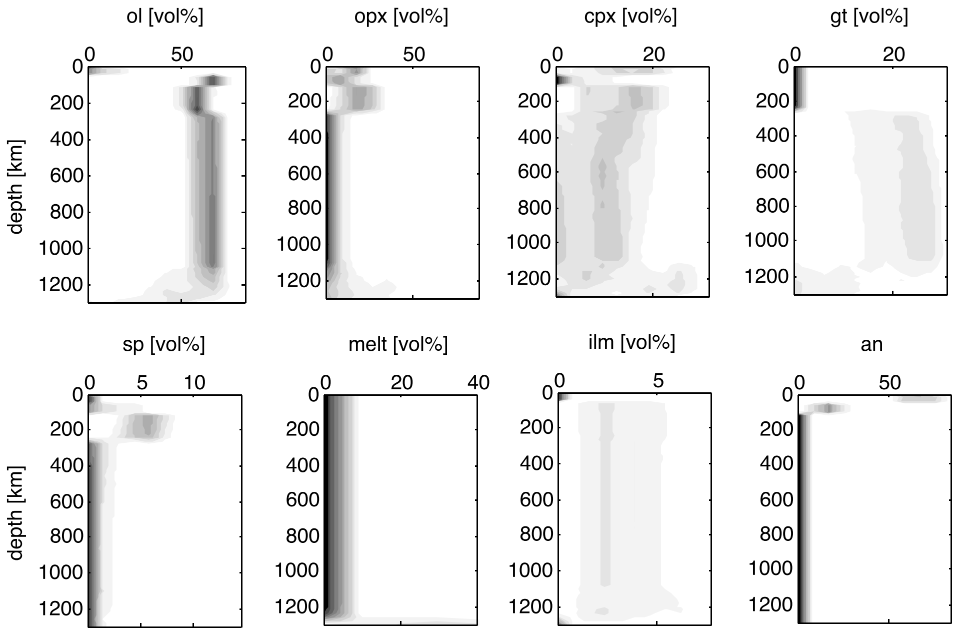

**Figure 11.** Inverted lunar mantle mineralogy. Phases are the following: ol (olivine), opx (orthopyroxene), cpx (clinopyroxene), gt (garnet), spinel (sp), melt (melt), ilmenite (ilm), and anothite (an).

pressure [*Wyatt*, 1977; *Longhi*, 2006]. These relatively high temperatures are supported by thermal modeling that takes into account the distribution of radiogenic heat-producing elements, e.g., U, K, and Th, in the various lunar magma ocean reservoirs [e.g., *de Vries et al.*, 2010]. In particular, the $TiO_2$-rich cumulates are enriched in U and Th providing the heat source required to maintain both supersolidus temperatures in the deep lunar interior and low core cooling rates. If the core cools too rapidly, mantle temperatures are influenced by plumes that rise from a layer surrounding the CMB. These plumes, however, do not transport dense ilmenite-rich material but only the less dense silicate material to the surface.

The existence of a present-day melt layer provides strong constraints on the thermal evolution of the magma ocean in that a number of dynamical requirements have to be met: (1) sinking of late-stage cumulates enriched in incompatible radiogenic heat-producing elements, (2) the formation of a stable layer from these cumulates, and (3) the stable layer has to remain molten to the present. The redistribution of heat-producing elements via their incompatible nature with the early lunar magma ocean cumulates that crystallize and their preferential incorporation into ilmenite and clinopyroxene and the extraction of these minerals toward the bottom as a result of late-stage cumulate overturn is clearly favored. In the absence of this process it is difficult to envisage how a melt layer would remain stably stratified to this day.

## 8. Summary and Concluding Remarks

As summarized in section 2 there is considerable geophysical evidence pointing to the presence of partial melt in the deep lunar interior. Geochemical analyses and petrological modeling likewise, albeit indirectly, support this scenario. This has been further strengthened here since we have demonstrated that in the absence of low shear modulus material in the deep Moon, the amount of dissipation required to fit the observed lunar Love number is not sufficient. The interpretation of this result is that it appears very likely that a melt layer resides within the deep lunar interior (depth range 1200–1400 km) that possibly surrounds the core. The case for the presence of melt above the lunar core-mantle boundary is also supported by recent evidence for a low-viscosity layer obtained from viscoelastic modeling. Although not discussed in any detail here, we might also mention that recent coupled thermal evolution models and dynamo simulations appear to require that the outer part of the core be molten at present [e.g., *Laneuville et al.*, 2013, 2014; *Zhang et al.*, 2013]. Refining these results will prove important for improving our understanding of lunar origin and evolution.

The results presented here have implications for lunar evolution. For a melt layer to persist to this day imparts strong constraints on thermal evolution models of the Moon. During lunar cumulate mantle overturn, toward the end of lunar magma ocean solidification, the sinking ilmenite-bearing cumulate layer must have incorporated and transported enough incompatible heat-producing elements to the bottom of the mantle for it to remain molten up until the present. Tidal dissipation of energy that appears to be localized to the partially molten region presents another prominent heat source. Moreover, presence of melt surrounding the core presents a viable means of maintaining the core, or at least its outer part, in a liquid state as strongly implied by analysis of LLR data [e.g., *Williams et al.*, 2001, 2012, 2014].

In relation to the thickness of the partially molten zone, the outer radius of the melt layer is smaller than originally inferred from observations of shear wave arrivals from farside deep moonquakes. *Nakamura et al.* [1973] had observed that the lone farside moonquake nest A33 produced strong *P* and *S* wave arrivals at the two closest stations (15 and 16), corresponding to bottoming depths of about 1000 km, while at the distant stations 12 and 14, corresponding to bottoming depths of around 1200 km, little-to-no shear wave energy was observed. These observations led to a shallower estimate of the depth of the partially molten region of ∼1000–1100 km relative to what is determined here. This is observed not only for A33, as reported earlier, but also for a few of the new farside nests A241 and A285 [*Nakamura*, 2005]. This suggests that either the A33 nest is significantly deeper than originally estimated or that because of a radially asymmetric lunar interior, the partial melt layer appears to be located shallower when observed far from the Apollo station network (Y. Nakamura, personal communication, 2014). Related to this is the suggestion that partial melts or fluid phases located subjacently to the deep moonquake source region might be responsible for producing deep moonquakes at pressures where ordinary brittle fracture is not possible [e.g., *Lammlein et al.*, 1974; *Frohlich and Nakamura*, 2009; *Weber et al.*, 2009]. However, if the melt is located well below the deep moonquake source region, this explanation will need to be modified, calling for other possible mechanisms [see *Frohlich and Nakamura*, 2009 for further details]. These issues will have to be investigated in more detail in the future.

In contrast to the model proposed here, *Nimmo et al.* [2012] have shown that a melt-free viscoelastically dissipating Moon, based on an extended Burgers rheological model and an olivine mineralogy, is also compatible with observed dissipation at tidal frequencies. In order to match tidal dissipation, Nimmo et al. found, assuming that viscous deformation in the lower mantle occurs through diffusion creep, that relatively large grain sizes in combination with temperatures in excess of 1400°C at the bottom of the mantle are needed to simultaneously satisfy the requirements of dissipation and absence of core-mantle boundary relaxation as suggested by LLR data [*Williams et al.*, 2001]. However, none of the models analyzed by Nimmo et al. were able to produce the frequency dependence of $Q$ indicated by LLR ($\alpha = -0.17 \pm 0.1$), which, if real, might possibly suggest that effects arising from melt cannot be overlooked (cf. viscoelastic modeling results of *Harada et al.* [2014]). Future studies will have to consider viscoelastic modeling in more detail, preferably posed in the form of an inverse problem.

We also remark that although the assumption here is that of an anhydrous lunar interior based on geochemical analyses and petrological modeling [e.g., *Elkins-Tanton and Grove*, 2011; *Hirschmann et al.*, 2012; *Tartése and Anand*, 2012], we have also considered the case where $C_w \neq 0$, i.e., the lunar hydrous case, when computing mineral conductivities (equations (3) and (4)). As regards the deep lunar melt layer we find little difference between the hydrous and anhydrous case. For the physical properties, particularly lunar geotherm and conductivity profile, we do observe small variations in the lunar upper mantle (depth range 200–600 km). However, these differences are relatively small amounting to <50°C and <0.1 log units, respectively, for water contents in the ranges $10^{-4}$–$10^{-2}$ wt % (olivine), $10^{-4.5}$–$10^{-2.5}$ wt % (orthopyroxene), and $10^{-5}$–$10^{-2}$ wt % (clinopyroxene).

In the context of a hydrous lunar mantle, the case has been made for the influence of water on the early thermal evolution of the Moon. *Evans et al.* [2014] find that a lunar lower mantle enriched in water will act to lower the viscosity thereby enabling an increased heat transport out of the deep mantle and the possibility of sustaining a core dynamo beyond 3.56 Ga. Previous mantle convection models were generally based on an anhydrous mantle and were unable to account for the heat flux across the core-mantle boundary that was needed in order that a core dynamo be operative for from 4.2–3.56 Ga [e.g., *Stegman et al.*, 2003; *Laneuville et al.*, 2013; *Zhang et al.*, 2013]. Water, if present today, could thus act as a mechanism for the continued presence of small amounts of melt in the deep lunar interior. However, more detailed modeling will be required to consider concomitant effects of water on phase equilibria and melting temperature, and we leave it for a future study to consider this further using improved data and analysis techniques [e.g., *Zhong et al.*, 2012]. Until acquisition of new lunar seismic data, continued improvement of analysis techniques and efforts to combine various data sets will likely prove the only means of making progress in understanding lunar structure and how this relates to its origin and evolution.

## Appendix A: Anelastic Correction to Tidal Love Number

The inversion presented here is based on computing mantle properties in the elastic limit, i.e., in the infinite-frequency limit. In contrast hereto, the observed Love number $k_2$ is obtained at a frequency of the lunar tide ($\sim\ 4 \cdot 10^{-7}$ Hz), where anelastic effects are nonnegligible [e.g., *Nimmo et al.*, 2012]. Therefore, prior to inversion the observed tidal Love number should be corrected for anelastic contributions in order that it is representative of purely elastic effects [e.g., *Zharkov and Gudkova*, 2005]. To this end, we adopt a Kelvin Earth model, i.e., an elastic incompressible homogeneous sphere, assumed to be valid in the seismic frequency range ($\sim$1 Hz) and derive a correction at tidal frequencies. For the aforementioned model, an analytical expression for $k_2$ can be derived due to Love [e.g., *Lambeck*, 1988]

$$k_2 = \frac{3}{2}\frac{1}{1+\mu'}, \qquad \mu' = \frac{19}{2}\frac{\mu}{\rho g R}, \tag{A1}$$

where $\mu, \rho, g$, and $R$ are bulk shear modulus, density, surface gravity, and radius, respectively. Using typical lunar values yields $\mu' \sim 100$, i.e., $\mu' \gg 1$, and the expression for $k_2$ (equation (A1)) reduces to

$$k_2 = \frac{3}{19}\frac{\rho g R}{\mu}, \tag{A2}$$

For the case of a weakly anelastic medium we assume that changes in $\mu$ and $k_2$ with frequency ($\omega$) outside of the seismic frequency band ($\omega_s$) are small and that dissipation occurs entirely in shear energy [e.g., *Wahr and Bergen*, 1986] and write

$$\mu(\omega) = \mu(\omega_s) + \delta\mu, \tag{A3}$$

$$k_2(\omega) = k_2(\omega_s) + \frac{\partial k_2}{\partial \mu}\delta\mu, \tag{A4}$$

$$= k_2(\omega_s) + \delta k_2 \tag{A5}$$

where $\omega\ <\ \omega_s$ and $\delta\mu$ and $\delta k_2$ represent small changes in $\mu$ and $k_2$ arising from anelasticity. Substituting equation (A2) into equation (A5) yields

$$k_2(\omega) = k_2(\omega_s)\left(2 - \frac{\mu(\omega)}{\mu(\omega_s)}\right). \tag{A6}$$

The dependence of shear modulus on frequency is given by [e.g., *Zharkov and Gudkova*, 2005]

$$\frac{\mu(\omega)}{\mu(\omega_s)} = 1 - \frac{1}{Q(\omega_s)}\left[\left(\frac{\omega_s}{\omega}\right)^{\alpha} - 1\right]\cot\frac{\alpha\pi}{2}, \tag{A7}$$

where the exponent $\alpha$ characterizes the frequency dependence of the quality factor $Q$ and is related to the physical process causing the dissipation

$$Q(\omega) = Q(\omega_s)\left(\frac{\omega}{\omega_s}\right)^{\alpha}. \tag{A8}$$

Based on seismic, geodetic, and laboratory studies [e.g., *Anderson and Minster*, 1979; *Smith and Dahlen*, 1981; *Sobolev et al.*, 1996; *Gribb and Cooper*, 1998; *Benjamin et al.* 2006; *Jackson and Faul*, 2010], $\alpha$ has been determined to be in the range 0.1–0.4. Substituting equations (A7) and (A8) into equation (A6) yields the anelastically corrected elastic tidal Love number $k_2$ at frequency $\omega_s$, which is deduced from the observed monthly tidal $k_2$ and $Q$ values at frequency $\omega_m$ ($\sim 4 \cdot 10^{-7}$ Hz)

$$k_2(\omega_s) = \frac{k_2(\omega_m)}{1 + \frac{1}{Q(\omega_m)}\left[1 - \left(\frac{\omega_m}{\omega_s}\right)^{\alpha}\right]\cot\frac{\alpha\pi}{2}}. \tag{A9}$$

**Acknowledgments**
We would like to thank two anonymous reviewers for their comments that led to a much improved manuscript. We are grateful to Jim Williams, Francis Nimmo, Yosio Nakamura, and John Wahr for discussions and to Bob Grimm, Shun Karato, John Longhi, Renee Weber and Oleg Kuskov for sharing their models. Numerical computations were performed on the ETH cluster Brutus.

## References

Anderson, D. L. (1989), Theory of the Earth, p. 279.

Anderson, D. L., and J. B. Minster (1979), The frequency dependence of Q in the Earth and implications for mantle rheology and Chandler wobble, *Geophys. J. R. Astron. Soc.*, *58*, 431–440.

Benjamin, D., J. Wahr, R. D. Ray, G. D. Egbert, and S. D. Desai (2006), Constraints on mantle anelasticity from geodetic observations, and implications for the $J_2$ anomaly, *Geophys. J. Int.*, *165*, 3–16, doi:10.1111/j.1365-246X.2006.02915.x.

Berryman, J. G. (1995), Mixture theories for rock properties, in *Rock Physics and Phase Relations: A Handbook of Physical Constants*, edited by T. J. Ahrens, pp. 205–228, AGU, Washington, D. C.

Besserer, J., F. Nimmo, M. A. Wieczorek, R. C. Weber, W. S. Kiefer, P. J. McGovern, J. C. Andrews-Hanna, D. E. Smith, and M. T. Zuber (2014), GRAIL gravity constraints on the vertical and lateral density structure of the lunar crust, *Geophys. Res. Lett.*, *41*, 5771–5777, doi:10.1002/2014GL060240.

Boyce, J. W., Y. Liu, G. R. Rossman, Y. Guan, J. M. Eiler, E. M. Stolper, and L. A. Taylor (2010), Lunar apatite with terrestrial volatile abundances, *Nature*, *466*, 466–469.

Circone, S., and S. B. Agee (1996), Compressibility of molten high-Ti mare glass: Evidence for crystal-liquid density inversions in the lunar mantle, *Geochim. Cosmochim. Acta*, *60*, 2709–2720.

Connolly, J. A. D. (2005), Computation of phase equilibria by linear programming: A tool for geodynamic modeling and an application to subduction zone decarbonation, *Earth Planet. Sci. Lett.*, *236*, 524–541.

Dai, L., H. Li, H. Hu, and S. Shan (2008), Experimental study of grain boundary electrical conductivities of dry synthetic peridotites under high temperature, high-pressure, and different oxygen fugacity conditions, *J. Geophys. Res*, *113*, B12211, doi:10.1029/2008JB005820.

Dai, L., and S.-I. Karato (2009a), Electrical conductivity of orthopyroxene: Implications for the water content of the asthenosphere, *Proc. Jpn. Acad.*, *85*, 466–475.

Dai, L., and S.-I. Karato (2009b), Electrical conductivity of pyrope-rich garnet at high temperature and pressure, *Phys. Earth Planet. Inter.*, *176*, 83–88, doi:10.1016/j.pepi.2009.04.002.

Dai, L., L. Heping, H. Hu, S. Shan, J. Jiang, and K. Hui (2012), The effect of chemical composition and oxygen fugacity on the electrical conductivity of dry and hydrous garnet at high temperatures and pressures, *Contrib. Mineral. Petrol.*, *163*, 689–700, doi:10.1007/s00410-011-0693-5.

Delano, J. W. (1986), Pristine lunar glasses: Criteria, data, and implications, *Proc. Lunar Planet. Sci. Conf. 16th, Part 2, J. Geophys. Res.*, *91*, D201–D213.

Delano, J. W. (1990), Buoyancy-driven melt segregation in the Earth's Moon. I: Numerical results, *Proc. Lunar Planet. Sci. Conf.*, *20*, 3–12.

de Vries, J., A. van den Berg, and W. van Westrenen (2010), Formation and evolution of a lunar core from ilmenite-rich magma ocean cumulates, *Earth Planet. Sci. Lett.*, *292*, 139–147, doi:10.1016/j.epsl.2010.01.029.

Duba, A. G., and S. Constable (1993), The electrical conductivity of Lherzolite, *J. Geophys. Res.*, *98*, 11,885–11,899.

Duba, A. G., and T. J. Shankland (1982), Free carbon and electrical conductivity in the Earth's mantle, *Geophys. Res. Lett.*, *9*, 1271–1274, doi:10.1029/GL009i011p01271.

Efroimsky, M. (2012), Tidal dissipation compared to seismic dissipation: In small bodies, earths, and super-earths, *Astrophys. J.*, *746*, 150.

Elkins-Tanton, L. T., J. Van Orman, B. H. Hager, and T. L. Grove (2002), Re-examination of the lunar magma ocean cumulate overturn hypothesis: Melting or mixing is required, *Earth Planet. Sci. Lett.*, *196*, 239–249.

Elkins-Tanton, L. T., N. Chatterjee, and T. Grove (2003), Experimental and petrological constraints on lunar differentiation from the Apollo 15 green picritic glasses, *Meteorit. Planet. Sci.*, *38*, 515–527.

Elkins-Tanton, L. T, and T. L. Grove (2011), Water (hydrogen) in the lunar mantle: Results from peteology and magma ocean modeling, *Earth Planet. Sci. Lett.*, *307*, 173–179, doi:10.1016/j/espl.2011.04.027.

Elkins-Tanton, L. T., S. Burgess, and Q.-Z. Yin (2011), The lunar magma ocean: Reconciling the solidification process with lunar petrology and geochronology, *Earth Planet. Sci. Lett.*, *304*, 326–336, doi:10.1016/j.epsl.2011.02.004.

Evans, A. J., M. T. Zuber, B. P. Weiss, and S. M. Tikoo (2014), A wet, heterogeneous lunar interior: Lower mantle and core dynamo evolution, *J. Geophys. Res. Planets*, *119*, 1061–1077, doi:10.1002/2013JE004494.

Frohlich, C., and Y. Nakamura (2009), The physical mechanisms of deep moonquakes and intermediate-depth earthquakes: How similar and how different?, *Phys. Earth Planet. Inter.*, *173*, 365–374, doi:10.1016/j.pepi.2009.02.004.

Garcia, R. F., J. Gagnepain-Beyneix, S. Chevrot, and P. Lognonné (2011), Very preliminary reference Moon model, *Phys. Earth Planet. Inter.*, *188*, 96–113, doi:10.1016/j.pepi.2012.03.009, doi:10.1016/j.pepi.2011.06.015. Erratum (2012), 202–203.

Garcia, R. F., J. Gagnepain-Beyneix, S. Chevrot, and P. Lognonné (2012a), Erratum to "Very Preliminary Reference Moon Model", by R. F. Garcia, J. Gagnepain-Beyneix, S. Chevrot, P. Lognonné [Phys. Earth Planet. Inter. 188 (2011) 96–113], *Phys. Earth Planet. Inter.*, *202*, 89–91, doi:10.1016/j.pepi.2012.03.009.

Garcia, R. F., J. Gagnepain-Beyneix, S. Chevrot, and P. Lognonné (2012b), Erratum to "Very Preliminary Reference Moon Model", by R. F. Garcia, J. Gagnepain-Beyneix, S. Chevrot, P. Lognonné [Phys. Earth Planet. Inter. 188 (2011) 96–113], *Phys. Earth Planet. Inter.*, *202*, 89–91, doi:10.1016/j.pepi.2012.03.009.

Ghiorso, M. S., M. M. Hirschmann, P. W. Reiners, and V. C. Kress (2002), The pMELTS: A revision of MELTS for improved calculation of phase relations and major element partitioning related to partial melting of the mantle to 3 GPa, *Geochem. Geophys. Geosyst.*, *3*(5), 1–35, doi:10.1029/2001GC000217.

Goossens, S., et al. (2011), Lunar gravity field determination using SELENE same-beam differential VLBI tracking data, *J. Geod.*, *85*, 205–228.

Gribb, T. T., and R. F. Cooper (1998), Low-frequency shear attenuation in polycrystalline olivine: Grain boundary diffusion and the physical significance of the Andrade model for viscoelastic rheology, *J. Geophys. Res.*, *103*, 27,267–27,279.

Greenwood, J. P., S. Itoh, N. Sakamoto, P. Warren, L. A. Taylor, and H. Yurimoto (2011), Hydrogen isotope ratios in lunar rocks indicate delivery of cometary water to the Moon, *Nat. Geosci.*, *4*, 79–82.

Grimm, R. E. (2013), Geophysical constraints on the lunar Procellarum KREEP Terrane, *J. Geophys. Res. Planets*, *118*, 768–777, doi:10.1029/2012JE004114.

Grimm, R. E., and G. T. Delory (2012), Next-generation electromagnetic sounding of the Moon, *Adv. Space Res.*, *50*, 1687–1701.

Haggerty, S. E. (1978), The redox state of planetary basalts, *Geophys. Res. Lett.*, *5*, 443–446.

Harada, Y., S. Goossens, K. Matsumoto, J. Yan, J. Ping, H. Noda, and J. Haruyama (2014), Strong tidal heating in an ultralow-viscosity zone at the core-mantle boundary of the Moon, *Nat. Geosci.*, *7*, 569–572, doi:10.1038/NGEO2211.

Hashin, Z., and S. Shtrikman (1962), A variational approach to the theory of effective magnetic permeability of multiphase materials, *J. Appl. Phys.*, *33*, 3125.

Hauri, E. H., T. Weinreich, A. E. Saal, M. C. Rutherford, and J. A. Van Orman (2011), High pre-eruptive water contents preserved in lunar melt inclusions, *Science*, *333*, 213–215.

Hess, P. (1991), Diapirism and the origin of high $TiO_2$ mare glasses, *Geophys. Res. Lett.*, *18*, 2069–2072.

Hess, P. C., and E. M. Parmentier (1995), A model for the thermal and chemical evolution of the Moon's interior: Implications for the onset of mare volcanism, *Earth Planet. Sci. Lett.*, *134*, 501–514.

Hirschmann, M. M. (2000), Mantle solidus: Experimental constraints and the effects of peridotite composition, *Geochem. Geophys. Geosys.*, *1*, 1042, doi:10.1029/2000GC000070.

Hirschmann, M. M. (2006), Water, melting, and the deep Earth $H_2O$ cycle, *Annu. Rev. Earth Planet. Sci.*, *34*, 629–653, doi:10.1146/annurev.earth.34.031405.125211.

Hirschmann, M. M., A. C. Withers, P. Ardia, and N. T. Foley (2012), Solubility of molecular hydrogen in silicate melts and consequences for volatile evolution of terrestrial planets, *Earth Planet. Sci. Lett.*, *345–348*, 38–48, doi:10.1016/j.epsl.2012.06.031.

Hobbs, B. A., L. L. Hood, F. Herbert, and C. P. Sonett (1983), An upper bound on the radius of a highly electrically conducting lunar core, *J. Geophys. Res.*, *88*, B97–B102.

Holland, T. J. B., and R. Powell (1998), An internally consistent thermodynamic data set for phases of petrological interest, *J. Metamorph. Geol.*, *16*, 309–343.

Hood, L. L., F. Herbert, and C. P. Sonett (1982), The deep lunar electrical conductivity profile: Structural and thermal inferences, *J. Geophys. Res.*, *87*, 5311–5326.

Hood, L. L., D. L. Mitchell, R. P. Lin, M. H. Acuna, and A. B. Binder (1999), Initial measurements of the lunar-induced magnetic dipole moment using Lunar Prospector magnetometer data, *Geophys. Res. Lett.*, *26*, 2327–2330.

Jackson, I., and U. H. Faul (2010), Grainsize-sensitive viscoelastic relaxation in olivine: Towards a robust laboratory-based model for seismological application, *Phys. Earth Planet. Inter.*, *183*, 151–163, doi:10.1016/j.pepi.2010.09.005.

Jackson, I., J. D. Fitz Gerald, U. H. Faul, and B. H. Tan (2002), Grain-łsizesensitive seismic wave attenuation in polycrystalline olivine, *J. Geophys. Res.*, *107*(B12), 2360, doi:10.1029/2001JB001225.

Jackson, I., U. Faul, J. FitzGerald, and B. Tan (2004), Shear wave attenuation and dispersion in melt-bearing olivine polycrystals: 1. Specimen fabrication and mechanical testing, *J. Geophys. Res.*, *109*, B06201, doi:10.1029/2003JB002406.

Jaumann, R., et al. (2012), Geology, geochemistry, and geophysics of the Moon: Status and current understanding, *Planet. Space Sci.*, *74*, 15–41.

Jones, J. H., and J. W. Delano (1989), A three-component model for the bulk composition of the moon, *Geochim. Cosmochim. Acta*, *53*(2), 513-527, doi:10.1016/0016-7037(89)90402-X.

Katsura, T., S. Yokoshi, K. Kawabe, A. Shatskiy, M. Okube, H. Fukui, E. Ito, A. Nozawa, and K.-I. Funakoshi (2007), Pressure dependence of electrical conductivity of (Mg, Fe)SiO3 ilmenite, *Phys. Chem. Miner.*, *34*, 249–255, doi:10.1007/s00269-007-0143-0.

Karato, S.-I. (2011), Water distribution across the mantle transition zone and its implications for global material circulation, *Earth Planet. Sci. Lett.*, *301*, doi:10.1016/j.epsl.2010.1.038.

Karato, S.-I. (2013), Geophysical constraints on the water content of the lunar mantle its implications for the origin of the Moon, *Earth Planet. Sci. Lett.*, *384*, 144–153, doi:10.1016/j.epsl.2013.10.001.

Karato, S., and D. Wang (2012), Electrical conductivity of minerals and rocks, in *Physics and Chemistry of the Deep Earth*, edited by S. Karato, pp. 145–182, Wiley-Blackwell, Hoboken, N. J.

Kesson, S. E., and A. E. Ringwood (1976), Mare basalt petrogenesis in a dynamic moon, *Earth Planet. Sci. Lett.*, *30*, 155–163.

Khan, A., and K. Mosegaard (2005), Further constraints on the deep lunar interior, *Geophys. Res. Lett.*, *32*, L22203, doi:10.1029/2005GL023985.

Khan, A., and T. J. Shankland (2012), A geophysical perspective on mantle water content and melting: Inverting electromagnetic sounding data using laboratory-based electrical conductivity profiles, *Earth Planet. Sci. Lett.*, *317–318*, 27–43, doi:10.1016/j.epsl.2011.11.031.

Khan, A., K. Mosegaard, J. G. Williams, and P. Lognonné (2004), Does the Moon possess a molten core? Probing the deep lunar interior using results from LLR and Lunar Prospector, *J. Geophys. Res.*, *109*, E09007, doi:10.1029/2004JE002294.

Khan, A., J. A. D. Connolly, N. Olsen, and K. Mosegaard (2006a), Constraining the composition and thermal state of the moon from an inversion of electromagnetic lunar day-side transfer functions, *Earth Planet. Sci. Lett.*, *248*, 579–598, doi:10.1016/j.epsl.2006.04.008.

Khan, A., J. Maclennan, S. R. Taylor, and J. A. D. Connolly (2006b), Are the Earth and the Moon compositionally alike?—Inferences on lunar composition and implications for lunar origin and evolution from geophysical modeling, *J. Geophys. Res.*, *111*, E05005, doi:10.1029/2005JE002608.

Khan, A., J. A. D. Connolly, J. Maclennan, and K. Mosegaard (2007), Joint inversion of seismic and gravity data for lunar composition and thermal state, *Geophys. J. Int.*, *168*, 243–258, doi:10.1111/j.1365-246X.2006.03200.x.

Khan, A., A. Pommier, and G. A. Neumann (2013), The lunar moho and the internal structure of the Moon: A geophysical perspective, *Tectonophysics*, *609*, 331–352, doi:10.1016/j.tecto.2013.02.024.

Klemme, S., T. J. Ivanic, J. A. D. Connolly, and B. Harte (2009), Thermodynamic modelling of Cr-bearing garnets with implications for diamond inclusions and peridotite xenoliths, *Lithos*, *112*, 986–991.

Konopliv, A., et al. (2013), The JPL lunar gravity field to spherical harmonic degree 660 from the GRAIL primary mission, *J. Geophys. Res. Planets*, *118*, 1415–1434, doi:10.1002/jgre.20097.

Kronrod, V. A., and O. L. Kuskov (2011), Inversion of seismic and gravity data for the composition and core size of the Moon, *Izv. Phys. Solid Earth*, *47*, 711–730, doi:10.1134/S1069351311070044.

Kuskov, O. L., and V. A. Kronrod (2009), Geochemical constraints on the model of the composition and thermal conditions of the Moon according to seismic data, *Izv. Phys. Solid Earth*, *45*, 753–768, doi:10.1134/S1069351309090043.

Kuskov, O. L., V. A. Kronrod, and L. L. Hood (2002), Geochemical constraints on the seismic properties of the lunar mantle, *Phys. Earth Planet. Inter.*, *143*, 175–189, doi:10.1016/S0031-9201(02)00156-5.

Kuskov, O. L., V. A. Kronrod, and E. V. Kronrod (2014), Thermo-chemical constraints on the interior structure and composition of the lunar mantle, *Phys. Earth Planet. Inter.*, *235*, 84–95, doi:10.1016/j.pepi.2014.07.011.

Lambeck, K. (1988), *Geophysical Geodesy: The Slow Deformation of the Earth*, 710 pp., Clarendon, Oxford, U. K.

Lammlein, D. R., G. V. Latham, J. Dorman, Y. Nakamura, and M. Ewing (1974), Lunar seismicity, structure, and tectonics, *Rev. Geophys. Space Phys*, *12*, 1–21.

Laneuville, M., M. A. Wieczorek, D. Breuer, and N. Tosi (2013), Asymmetric thermal evolution of the Moon, *J. Geophys. Res. Planets*, *118*, 1435–1452, doi:10.1002/jgre.20103.

Laneuville, M., M. A. Wieczorek, D. Breuer, J. Aubert, and G. Morard (2014), A long-lived lunar dynamo powered by core crystallization, *Earth Planet. Sci. Lett.*, *401*, 251–260, doi:10.1016/j.epsl.2014.05.057.

Landauer, R. (1952), The electrical resistance of binary metallic mixtures, *J. Appl. Phys.*, *23*, 779–784.

Lemoine, F. G., et al. (2013), High-degree gravity models from GRAIL primary mission data, *J. Geophys. Res. Planets*, *118*, 1676–1698, doi:10.1002/jgre.20118.

Lognonné, P., and C. L. Johnson (2007), Planetary seismology, in *Treatise in Geophysics*, vol. 10, chap. 4, edited by G. Schubert, pp. 69–122, Esevier, Oxford, U. K.

Longhi, J. (1992), Origin of picritic green glass magmas by polybaric fractional fusion, in *Proc. Lunar Planet. Sci. Conf., Houston, Tex., 18-22 March 1991*, vol. 22, pp. 343–353, Lunar and Planet. Inst., Houston, Tex.

Longhi, J. (2003), A new view of lunar ferroan anorthosites: Postmagma ocean petrogenesis, *J. Geophys. Res.*, *108*(E8), 5083, doi:10.1029/2002JE001941.

Longhi, J. (2006), Petrogenesis of picritic mare magmas: Constraints on the extent of early lunar differentiation, *Geochim. Cosmochim. Acta*, *70*, 5919–5934, doi:10.1016/j.gca.2006.09.023.

Mosegaard, K., and A. Tarantola (1995), Monte Carlo sampling of solutions to inverse problems, *J. Geophys. Res.*, *100*, 12,431–12,447.

Nakamura, Y. (2003), New identification of deep moonquakes in the Apollo lunar seismic data, *Phys. Earth Planet. Inter.*, *139*, 197–205.

Nakamura, Y. (2005), Farside deep moonquakes and deep interior of the Moon, *J. Geophys. Res.*, *110*, E01001, doi:10.1029/2004JE002332.

Nakamura, Y. (2010), Lunar seismology: Current status and future challenges, *Dtsch. Geophys. Ges. Mitt.*, *3*, 4–13.

Nakamura, Y., D. Lammlein, G. Latham, M. Ewing, J. Dorman, F. Press, and M. Toksöz (1973), New seismic data on the state of the deep lunar interior, *Science*, *181*, 49–51.

Nakamura, Y., G. Latham, D. Lammlein, M. Ewing, F. Duennebier, and J. Dorman (1974), Deep lunar interior inferred from recent seismic data, *Geophys. Res. Lett.*, *1*, 137–140.

Nimmo, F., U. H. Faul, and E. J. Garnero (2012), Dissipation at tidal and seismic frequencies in a melt-free Moon, *J. Geophys. Res.*, *117*, E09005, doi:10.1029/2012JEE004160.

Poe, B., C. Romano, F. Nestola, and J. R. Smyth (2010), Electrical conductivity anisotropy of dry and hydrous olivine at 8 GPa, *Phys. Earth Planet. Inter.*, *181*, 103–111.

Pommier, A., and E. Le Trong (2011), "SIGMELTS": A web portal for electrical conductivity calculations in geosciences, *Comput. Geosci.*, *37*, 1450–1459, doi:10.1016/j.cageo.2011.01.002.

Pommier, A., F. Gaillard, M. Malki, and M. Pichavant (2010), Reevaluation of the electrical conductivity of silicate melts, *Am. Mineral.*, *95*, 284–291.

Romano, C., B. Poe, N. Kreidie, and C. McCammon (2006), Electrical conductivities of pyrope-almandine garnets up to 19 GPa and 1700°C, *Am. Mineral.*, *91*, 1371–1377.

Roberts, J. J., and J. A. Tyburczy (1993), Impedance spectroscopy of single and polycrystalline olivine: Evidence for grain boundary transport, *Phys. Chem. Miner.*, *20*, 19–26, doi:10.1007/BF00202246.

Saal, A. E., E. H. Hauri, M. L. Cascio, J. A. van Orman, M. C. Rutherford, and R. F. Cooper (2008), Volatile content of lunar volcanic glasses and the presence of water in the Moon's interior, *Nature*, *454*, 192–195, doi:10.1038/nature07047.

Sakamaki, T., E. Ohtani, S. Urakawa, A. Suzuki, Y. Katayama, and D. Zhao (2010), Density of high-Ti basalt magma at high pressure and origin of heterogeneities in the lunar mantle, *Earth Planet. Sci. Lett.*, *299*, 293–297, doi:10.1016/j.epsl.2010.09.007.

Sellers, P. (1992), Seismic evidence for a low-velocity lunar core, *J. Geophys. Res.*, *97*, 11,663–11,672.

Schock, R. N., A. G. Duba, and T. J. Shankland (1989), Electrical conduction in olivine, *J. Geophys. Res.*, *94*, 5829–5839.

Shankland, T. J., and H. S. Waff (1977), Partial melting and electrical conductivity anomalies in the upper mantle, *J. Geophys. Res.*, *82*, 5409–5417.

Shearer, C. K., and J. J. Papike (1999), Magmatic evolution of the Moon, *Am. Mineral.*, *84*, 1469–1494.

Shearer, C. K., J. J. Papike, K. C. Galbreath, and N. Shimizu (1991), Exploring the lunar mantle with secondary ion mass spectrometry: A comparison of lunar picritic glass beads from the Apollo 14 and Apollo 17 sites, *Earth Planet. Sci. Lett.*, *102*, 134–147.

Shearer, C. K., et al. (2006), Thermal and magmatic evolution of the Moon, in *New Views of the Moon. Reviews in Mineralogy and Geochemistry*, vol. 60, edited by B. L. Jolliff et al., pp. 365–518, Mineralog. Soc. Am., Chantilly, Va.

Shimizu, H., M. Matsushima, F. Takahashi, H. Shibuya, and H. Tsunakawa (2013), Constraint on the lunar core size from electromagnetic sounding based on magnetic field observations by an orbiting satellite, *Icarus*, *222*, 32–43, doi:10.1016/j.icarus.2012.10.029.

Smith, J. R., and C. B. Agee (1997), Compressibility of molten "green glass" and crystal-liquid density inversions in low-Ti lunar magma, *Geochim. Cosmochim. Acta*, *61*, 2139–2145.

Smith, M. L., and F. A. Dahlen (1981), The period and $Q$ of the Chandler wobble, *Geophys. J. R. Astron. Soc.*, *64*, 223–281.

Sato, M., and N. L. Hickling (1973), Oxygen fugacity values of Apollo 12, 14, and 15 lunar samples and reduced state of lunar magmas, in *Proceedings 4th Lunar Sci. Conf., Houston, Tex., 5–8, March*, vol. 1, pp. 1061–1079, Pergamon Press, New York.

Snyder, G. A., L. A. Taylor, and C. R. Neal (1992), A chemical model for generating the sources of mare basalts: Combined equilibrium and fractional crystallization of the lunar magma-sphere, *Geochim. Cosmochim. Acta*, *56*, 3809–3823.

Sobolev, S. V., H. Zeyen, G. Stoll, F. Werling, R. Altherr, and K. Fuchs (1996), Upper mantle temperatures from teleseismic tomography of French Massif Central including effects of composition, mineral reactions, anharmonicity, anelasticity and partial melt, *Earth Planet. Sci. Lett.*, *139*, 147–163.

Sonett, C. P. (1982), Electromagnetic induction in the Moon, *Rev. Geophys. Space Phys.*, *20*, 411–455.

Stacey, F. D., and D. L. Anderson (2001), Electrical and thermal conductivities of Fe-Ni-Si alloy under core conditions, *Phys. Earth Planet. Inter.*, *124*, 153–162.

Stegman, D. R., A. M. Jellinek, S. A. Zatman, J. R. Baumgardner, and M. A. Richards (2003), An early lunar core dynamo driven by thermochemical mantle convection, *Nature*, *421*, 143–146, doi:10.1038/nature01267.

Tartése, R., and M. Anand (2012), Late delivery of chondritic hydrogen into the lunar mantle: Insights from mare basalts, *Earth Planet. Sci. Lett.*, *361*, 480–486, doi:10.1016/j.epsl.2012.11.015.

Taylor, S. R. (1982), *Planetary Science: A Lunar Perspective*, LPI, Houston, Tex.

Taylor, S. R. (2014), The Moon re-examined, *Geochim. Cosmochim. Acta*, *141*, 670–676, doi:10.1016/j.gca.2014.06.031.

Taylor, S. R., and P. Jakes (1974), The geochemical evolution of the Moon, in *Proc. Lunar Sci. Conf. 5th, Houston, Tex.*, 18–22 March 1974, pp. 1287–1305, Pergamon Press, New York.

Taylor, S. R, G. J. Taylor, and L. A. Taylor (2006), The Moon: A Taylor perspective, *Geochim. Cosmochim. Acta*, *70*, 5903–5918.

ten Grotenhuis, S. M., M. R. Drury, C. J. Peach, and C. J. Spiers (2004), Electrical properties of fine-grained olivine: Evidence for grain boundary transport, *J. Geophys. Res*, *109*, B06203, doi:10.1029/2003JB002799.

Toffelmier, D. A., and J. A. Tyburczy (2007), Electromagnetic detection of a 410-km-deep melt layer in the southwestern United States, *Nature*, *447*, 991–994, doi:10.1038/nature05922.

Tyburczy, J. A., and D. K. Fisler (1995), Electrical properties of minerals and melts, in *Mineral Physics and Crystallography: A Handbook of Physical Constants*, edited by T. J. Ahrens, p. 185, AGU, Washington, D. C.

van Kan Parker, M., C. B. Agee, M. S. Duncan, and W. van Westrenen (2011), Compressibility of molten Apollo 17 orange glass and implications for density crossovers in the lunar mantle, *Geochim. Cosmochim. Acta*, *75*, 1161–1172, doi:10.1016/j.gca.2010.11.022.

van Kan Parker, M., C. Sanloup, N. Sator, B. Guillot, E. J. Tronche, J.-P. Perrillat, M. Mezouar, N. Rai, and W. van Westrenen (2012), Neutral buoyancy of titanium-rich melts in the deep lunar interior, *Nat. Geosci.*, *5*, 186–189, doi:10.1038/ngeo1402.

Wagner, T. P., and T. L. Grove (1997), Experimental constraints on the origin of lunar high-Ti ultramafic glasses, *Geochim. Cosmochim. Acta*, *61*, 1315–1327.

Wahr, J. M., and Z. Bergen (1986), The effects of mantle anelasticity on nutations, Earth tides and tidal variations in rotation rate, *Geophys. J. R. Astron. Soc.*, *87*, 633.

Wang, D., M. Mookherjee, Y. Xu, and S.-I. Karato (2006), The effect of water on the electrical conductivity in olivine, *Nature*, *443*, 977–980.

Warren, P. H. (2005), "New" lunar meteorites: Implications for composition of the global lunar surface, lunar crust, and the bulk Moon, *Meteorit. Planet. Sci.*, *40*, 477–506.

Watson, H. C., J. J. Roberts, and J. A. Tyburczy (2010), The effect of conductive grain boundary impurities on electrical conductivity in polycrystalline olivine, *Geophys. Res. Lett.*, *37*, L02303, doi:10.1029/2009GL041566.

Weber, R. C., B. G. Bills, and C. L. Johnson (2009), Constraints on deep moonquake focal mechanisms through analyses of tidal stress, *J. Geophys. Res.*, *114*, E05001, doi:10.1029/2008JE003286.

Weber, R. C., P.-Y. Lin, E. J. Garnero, Q. Williams, and P. Lognonné (2011), Seismic detection of the lunar core, *Science*, *331*, 309–312, doi:10.1126/science.1199375.

Wieczorek, M. A., et al. (2006), The constitution and structure of the lunar interior, *Rev. Mineral. Geochem.*, *60*, 221—364, doi:10.2138/rmg.2006.60.3.

Wieczorek, M. A., et al. (2013), The crust of the Moon as seen by GRAIL, *Science*, *339*, 671–675, doi:10.1126/science.1231530.

Williams, J. G., D. H. Boggs, C. F. Yoder, J. T. Radcliff, and J. O. Dickey (2001), Lunar rotational dissipation in solid body and molten core, *J. Geophys. Res.*, *106*, 27,933–27,968.

Williams, J. G., D. H. Boggs, and J. T. Ratcliff (2012), Lunar moment of inertia, Love number and core, Abstract 2230 paper presented at 43rd Lunar and Planetary Science Conference, Lunar and Planetary Institute, Houston.

Williams, J. G., et al. (2014), Lunar interior properties from the GRAIL mission, *J. Geophys. Res. Planets*, *119*, 1546–1578, doi:10.1002/2013JE004559.

Wood, B. J., and J. R. Holloway (1984), A thermodynamic model for subsolidus equilibria in the system CaO-MgO-Al2O3-SiO2, *Geochim. Cosmochim. Acta*, *66*, 159–176.

Xu, Y., T. J. Shankland, and B. T. Poe (2000a), Laboratory-based electrical conductivity in the Earth's mantle, *J. Geophys. Res.*, *105*, 27,865–27,875.

Xu, Y., T. J. Shankland, and A. G. Duba (2000b), Pressure effect on electrical conductivity of mantle olivine, *Phys. Earth Planet. Inter.*, *118*, 149–161.

Yan, J., et al. (2011), CEGM02: An improved lunar gravity model using Chang'E-1 orbital tracking data, *Planet. Space Sci.*, *62*, 1–9, doi:10.1016/j.pss.2011.11.010.

Yang, X., H. Keppler, C. McCammon, H. Ni, O. Xia, and Q. Fan (2011), Effect of water on the electrical conductivity of lower crustal clinopyroxene, *J. Geophys. Res.*, *116*, B04208, doi:10.1029/2010JB008010.

Yang, X., H. Keppler, C. McCammon, and H. Ni (2012), Electrical conductivity of orthopyroxene and plagioclase in the lower crust, *Contrib. Mineral. Petrol.*, *163*, 33–48, doi:10.1007/s00410-011-0657-9.

Yoshino, T. (2010), Laboratory electrical conductivity measurements of mantle minerals, *Surv. Geophys*, *31*, 163–206.

Yoshino, T., M. Nishi, T. Matsuzaki, D. Yamazaki, and T. Katsura (2008), Electrical conductivity of majorite garnet and its implications for electrical structure in the mantle transition zone, *Phys. Earth Planet. Inter.*, *170*, 193–200, doi:10.1016/j.pepi.2008.04.009.

Yoshino, T., T. Matsuzaki, A. Shatskiy, and T. Katsura (2009), The effect of water on the electrical conductivity of olivine aggregates and its implications for the electrical structure of the upper mantle, *Earth Planet. Sci. Lett.*, *288*, 291–300, doi:10.1016/j.epsl.2009.09.032.

Yoshino, T., M. Laumonier, E. McIsaac, and T. Katsura (2010), Electrical conductivity of basaltic and carbonatite melt-bearing peridotites at high pressures: Implications for melt distribution and melt fraction in the upper mantle, *Earth Planet. Sci. Lett.*, *295*, 593–602, doi:10.1016/j.epsl.2010.04.050.

Zhang, N., E. M. Parmentier, and Y. Liang (2013), A 3-D numerical study of the thermal evolution of the Moon after cumulate mantle overturn: The importance of rheology and core solidification, *J. Geophys. Res. Planets*, *118*, 1789–1804, doi:10.1002/jgre.20121.

Zharkov, V. N., and T. V. Gudkova (2005), Construction of Martian interior model, *Sol. Syst. Res.*, *39*, 343–373.

Zhong, S., C. Qin, A. Geruo, and J. Wahr (2012), Can tidal tomography be used to unravel the long-wavelength structure of the lunar interior?, *Geophys. Res. Lett.*, *39*, L15201, doi:10.1029/2012GL052362.